J. Fluid Mech. (2004), *vol.* 516, *pp.* 181–209. © 2004 Cambridge University Press
DOI: 10.1017/S0022112004000485 Printed in the United Kingdom

Convection driven by differential heating at a horizontal boundary

By JULIA C. MULLARNEY, ROSS W. GRIFFITHS AND GRAHAM O. HUGHES

Research School of Earth Sciences, Australian National University, Canberra, ACT 0200, Australia

(Received 14 October 2003 and in revised form 16 February 2004)

We report laboratory and numerical experiments with the convective circulation that develops in a long channel driven by heating and cooling through opposite halves of the horizontal base. The problem is similar to that posed by Stommel (*Proc. Natl Acad. Sci.* vol. 48, 1962, p. 766) and Rossby (*Deep-Sea Res.* vol. 12, 1965, p. 9; *Tellus* vol. 50, 1998, p. 242), where flow forced by a linear temperature variation along the ocean surface or the base of a tank presented a demonstration of the smallness of sinking regions in the meridional overturning circulation of the oceans. In contrast to the previous experiments, we use small aspect ratio, larger Rayleigh numbers, piecewise uniform boundary conditions and an imposed input heat flux. The flow is characterized by a vigorous overturning circulation cell filling the box length and depth. A stable thermocline forms above the cooled base and is advected over the heated part of the base, where it is eroded from below by small-scale three-dimensional convection, forming a 'convective mixed layer'. At the endwall, the convective mixing is overshadowed by a narrow but turbulent plume rising through the full depth of the box. The return flow along the top of the box is turbulent with large slowly migrating eddies, and occupies approximately a third of the total depth. Theoretical scaling laws give temperature differences, thermocline thickness and velocities that are in good agreement with the experimental data and two-dimensional numerical solutions. The measured and computed density structure is largely similar to the thermocline and abyssal stratification in the oceans.

1. Introduction

The flows resulting from a horizontal difference in temperature or heat flux at a single horizontal boundary of a fluid have become known as 'horizontal convection'. The flows are very different from the more familiar Rayleigh–Bénard and Grashof forms of convection that carry heat between two horizontal or vertical boundaries. In horizontal convection, the heat flux does not necessarily have to be transported through the fluid depth. Indeed, it has been thought that only a slow diffusively-driven circulation can develop near the level of the heat source and sink (Jeffreys 1925; Huang 1999), although laboratory experiments with a horizontal temperature gradient have demonstrated a circulation filling the depth of the box (Rossby 1965). Horizontal convection has received relatively little attention, particularly from experimentalists, but may have much to teach us about the dynamics of the deep overturning circulation of the oceans and the role of surface buoyancy fluxes.

A simple conceptual model for the meridional overturning component of the ocean circulation is the convective flow driven by a horizontal surface temperature gradient (Stommel 1962). The meridional overturning circulation (also referred to as the global

https://doi.org/10.1017/S0022112004000485 Published online by Cambridge University Press

thermohaline circulation) of the oceans advects warm subtropical surface waters to high latitudes, where it cools and sinks. In the present pattern of circulation, the dense cold (and sufficiently saline) water sinks in confined regions at high latitudes to form 'Deep' and 'Bottom' waters (see e.g. Warren 1981). It is hypothesized that there is a slow, possibly basin-wide, upwelling to the surface to match the poleward mass flux, with the loop closed by a zonal average return flow toward the equator at depths below the thermocline. The strength of the circulation and the heat transport must depend on the rate of vertical diffusion of heat (Munk 1966; Bryan & Cox 1967; Munk & Wunsch 1998; Wunsch & Ferrari 2004). In the oceans the diffusion is believed to be caused by breaking internal waves and turbulent mixing processes (energized by winds and tides, Munk & Wunsch 1998), which act to increase the potential energy of the water column. The resulting heat flux carried by the overturning circulation has a significant role in the climate system, and changes in this circulation have been implicated as a cause of climate variability on decadal to millennial timescales.

A non-rotating two-dimensional form of this flow was realized in laboratory experiments (Rossby 1965) and in related numerical solutions (Rossby 1998), where a linear temperature gradient was imposed along the base of a water tank. The resulting flow exhibited an extreme asymmetry between the size of the sinking and rising legs of the convective overturning, with upward motion being confined to a narrow plume against the endwall above the hot end of the base, where the water has the lowest density in the box. In those experiments and computations, the ratio of box height to length was 1 : 2.5 and 1 : 1, respectively, while the horizontal Rayleigh number (based on the box length) ranged up to 10^8. The flow was laminar. In the work reported here, we extend experiments and computed solutions to larger Rayleigh numbers and a smaller aspect ratio, but with thermal boundary conditions that are more convenient to achieve in the laboratory. We observe two new features of the flow: vertical mixing by small-scale convection, and turbulent shear flow in both the plume and the weakly stratified return flow of the interior.

Rossby (1965) concluded that the interior water is warmed by advection of heat from, and cooled by diffusion to, the forcing boundary. The resulting asymmetry in the flow was attributed to the relative efficiencies of the two heat transfer processes, although Winton (1995) and Marotzke & Scott (1999) pointed out that the vertical advection acts on a very small vertical temperature gradient while the diffusion acts on a relatively large stable gradient, and therefore different efficiencies do not in themselves explain the smallness of the sinking regions and much larger area required for the diffusive transport. We add that the transport of heat both to and from the boundary, under the conditions studied, was by diffusion into a laminar boundary layer. Nevertheless, the upwelling plume ensures that the interior temperature far from the forcing boundary is very close to that of the water against the base at the hot end of the box, and these are the highest temperatures in the box. In the ocean context (i.e. turning the experiment upside down, adding rotation and using a stress-free surface), Winton (1995) used a general circulation model (GCM) to show that solutions having narrow sinking regions correspond to minimum potential energy, maximum downward diffusion of heat, maximum baroclinic horizontal pressure gradient and maximal overturning strength compared to less asymmetric states carrying the same heat flux.

The laboratory flows involve a balance over most of the horizontal area, excepting the small area of upwelling, between the downward diffusive transport of heat in the cold thermocline (i.e. upward growth of the thermocline) and the slow downward advection of warm water. The lateral flow in the boundary layer is characterized by a buoyancy-friction momentum balance. Thus, the flow is forced (both in terms of

https://doi.org/10.1017/S0022112004000485 Published online by Cambridge University Press

momentum and energy) entirely by buoyancy, with the strength of the circulation dependent on both the boundary temperature difference (or heat flux) and the vertical diffusivity. These dynamics in the experimental flow are fundamentally different from those suggested by Munk & Wunsch (1998) and Huang (1999) for the oceanic overturning (see also the review by Wunsch & Ferrari 2004): these authors argue that the primary energy source for the meridional overturning is the turbulent mechanical energy, which in turn, is derived from external sources (tidal and wind-driven motion), rather than the surface buoyancy fluxes. It was also concluded that the heat transport is an 'incidental' consequence of the overturning – a conclusion that appears to leave only the surface wind stress to provide the driving force that gives momentum to the mean overturning. An alternative dynamic is that interior mixing in the oceans (whether energized by winds, tides or buoyancy fluxes) again governs the uptake of buoyancy and generation of available potential energy, while the overturning circulation is generated by the buoyancy forces produced by surface heat and water fluxes. It is therefore important to examine the flow dynamics in the purely buoyancy-driven case. Also of interest is the added possibility that a significant portion of the interior turbulent mixing may be generated by the surface buoyancy fluxes.

Rossby (1965) derived a boundary-layer scaling analysis of non-rotating 'horizontal convection' and predicted that the Nusselt number Nu is proportional to the Rayleigh number Ra according to $Nu \sim Ra^{1/5}$ (where Ra is based on the applied end-to-end temperature difference). The predicted boundary-layer thickness h varies as $Ra^{-1/5}$. These scaling results were consistent with the laboratory data and two-dimensional numerical solutions for large Prandtl number, Rayleigh numbers up to 10^8 and an aspect ratio of one (Rossby 1998) (although they may not be valid for the case of a stress-free forcing boundary; W. R. Young, personal communication). Paparella & Young (2002) solved numerically the two-dimensional flow for a minimum top boundary temperature at the centre of the box and a maximum temperature above both ends, giving a downwelling plume at the centre. They examined the flow at higher Rayleigh numbers, smaller Prandtl numbers and an aspect ratio of 1:4, and found a transition to unsteady two-dimensional eddying flow (at a Rayleigh number which increased with Prandtl number). Paparella & Young (2002) also predicted that the box-averaged rate of viscous dissipation $\overline{\epsilon}$ per unit mass is given by the expression

$$\overline{\epsilon} = \left(\frac{\kappa g}{D\rho_0}\right)(\overline{\rho}_b - \overline{\rho}_t), \tag{1.1}$$

where κ is the molecular diffusivity for density that controls the uptake of buoyancy at the boundary, $\overline{\rho}_b$ and $\overline{\rho}_t$ are the horizontally averaged densities at the bottom and top boundaries, respectively, ρ_0 is a reference density, and D is the box depth. From this they inferred that the flow must be non-turbulent for vanishing molecular diffusivity (at a fixed Prandtl number). The same conclusion will apply for very large box depth.

The dynamics and pattern of ocean circulation are strongly influenced by planetary rotation and surface wind stress. This makes the flow three-dimensional, largely geostrophic, and introduces the process of vertical Ekman pumping. Scaling laws assuming geostrophic balance (Bryan & Cox 1967; Park & Bryan 2000) are expected to be more appropriate than the buoyancy–viscous scaling, and give a different dependence of heat flux on vertical diffusivity. Ekman pumping may overshadow diffusion within some part of the surface boundary layer. However, the fundamental point is that both the rotating and non-rotating models predict that the strength of the overturning depends on the thermal forcing and the vertical diffusivity, and they pose

https://doi.org/10.1017/S0022112004000485 Published online by Cambridge University Press

the common question of whether external energy supply (beyond the potential energy available from buoyancy fluxes) is necessary to provide enhanced diffusion in the deep interior and to uptake the buoyancy from the surface.

Investigation of the rotating case has been confined largely to general circulation models (e.g. Bryan & Cox 1967; Bryan 1987; Colin de Verdiere 1988; Wright & Stocker 1991; Winton 1995; Marotzke 1997; Park & Bryan 2000, 2001), in which convective mixing must be crudely parameterized by using convective adjustment or enhanced vertical diffusion schemes, and in which there are uncertainties resulting from spatial resolution and effective numerical diffusivity. Laboratory experiments with rotating horizontal convection include the case with heating and cooling through vertical endwalls of a long tank (Condie & Ivey 1988; Condie & Griffiths 1989) – this is a system in which there is no region of stabilizing boundary flux, the convection is actively forced through the full depth of the box, and the flow is symmetric. In another experiment, a heating flux was applied over a fifth of the base in a strip along one end of a rectangular box while cooling with a prescribed temperature was applied over a fifth of the base at the opposite end (Park & Whitehead 1999). The thickness of the thermal boundary layer and the meridional temperature difference in the flow were functions of the imposed heat flux and Coriolis parameter (i.e. the Rayleigh and Ekman numbers), and were consistent with the predictions of the Bryan & Cox (1967) scaling laws.

In this paper we return to the non-rotating case and report new experimental observations of turbulent flow in the endwall plume and the interior. The experiments also show how small-scale three-dimensional convection can cause vertical mixing near the forcing surface and the formation of a mixed layer within the two-dimensional large-scale circulation. As far as we are aware, this is the first report of convective mixing and turbulent interior motion in horizontal convection. These observations involve new conditions, particularly a small depth-to-length aspect ratio for the box ($D/L = 0.16$), approximately piecewise uniform boundary conditions on the base, and a range of Rayleigh numbers larger than those used previously (we use $6.5 \times 10^{12} \leqslant Ra_F \leqslant 6.84 \times 10^{14}$, where Ra_F is based on the applied input heat flux and box length). These changes are likely to create conditions more favourable to small-scale instability compared with those employed by Rossby (1965). Another difference is that we impose a heat flux. However, our additional runs with an imposed temperature difference reveal the same behaviour. We also present complementary two-dimensional numerical solutions obtained from a finite-volume code.

The problem and governing equations are defined in § 2, where we also give a boundary-layer analysis and scaling laws for the flow. The laboratory apparatus and methods are described in § 3 and the results given in § 4. In § 5 we present a very simple model for the development of the convective mixed layer. Two-dimensional numerical solutions are given in § 6. Our conclusions and some implications for the oceans are discussed in § 7.

2. Theoretical analysis

2.1. *Governing equations*

We consider a convective flow in a long rectangular box (figure 1). A uniform heat flux per unit area, F_T (in $\mathrm{W\,m^{-2}}$), is imposed over the left-hand half of the base and a uniform temperature is imposed over the right-hand half of the base. Instead of applying a temperature gradient along the base, we impose a uniform flux boundary condition at the heated end because it is experimentally more convenient (a linear temperature gradient is difficult to achieve over a distance of order 1 m) and allows

https://doi.org/10.1017/S0022112004000485 Published online by Cambridge University Press

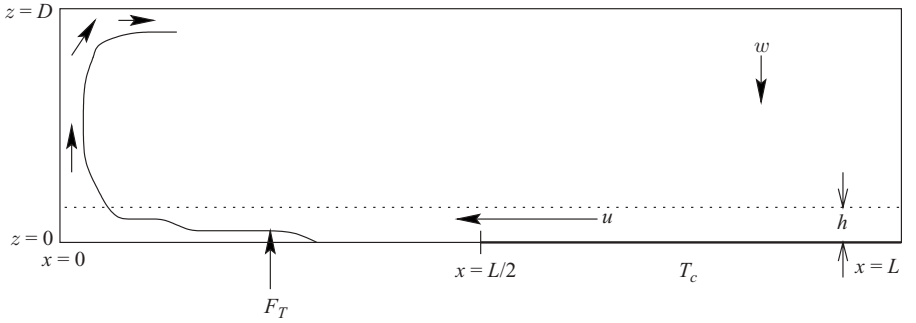


FIGURE 1. Sketch of flow in a vertical plane through the box. There is a slow downwelling velocity w throughout most of the interior, and a boundary layer of depth h across the cooled part of the base. F_T is the heat flux per unit area imposed over the left-hand half of the base and T_c is the temperature on the cooled part of the base ($L/2 < x \leqslant L$). The resulting interior temperature is T_0. The solid curve denotes the boundaries of the convective mixed layer and the upwelling plume (§ 4.2).

a more accurate determination of the heat flux into the fluid. All other boundaries are assumed to be perfect insulators and all boundary conditions are constant. In thermal equilibrium, heat is removed through the cooled half of the base at a rate that is equal to the total heat input at the heated end. Thus, the imposed flux controls the strength of convection and the magnitude of the temperature differences in the flow, whereas the temperature imposed over the cold half of the base controls the absolute temperature in the box.

The governing equations and a boundary-layer analysis of the problem are similar to that given by Rossby (1965) for a linear imposed temperature variation along the base. For this study, we change the boundary conditions and use a scaling based on the imposed heat flux. The flow is assumed to be Boussinesq and two-dimensional. Velocities in the horizontal (x) and vertical (z) directions are denoted by u and w, respectively. The equations for momentum, mass conservation, heat and density are:

$$\frac{\partial u}{\partial t} + u\frac{\partial u}{\partial x} + w\frac{\partial u}{\partial z} = -\frac{1}{\rho_0}\frac{\partial p}{\partial x} + \nu\nabla^2 u, \tag{2.1}$$

$$\frac{\partial w}{\partial t} + u\frac{\partial w}{\partial x} + w\frac{\partial w}{\partial z} = -\frac{1}{\rho_0}\frac{\partial p}{\partial z} + \nu\nabla^2 w - \frac{\rho}{\rho_0}g, \tag{2.2}$$

$$\frac{\partial u}{\partial x} + \frac{\partial w}{\partial z} = 0, \tag{2.3}$$

$$\frac{\partial T}{\partial t} + u\frac{\partial T}{\partial x} + w\frac{\partial T}{\partial z} = \kappa_T\nabla^2 T, \tag{2.4}$$

$$\frac{\rho}{\rho_0} = 1 - \alpha(T - T_0). \tag{2.5}$$

Here, ρ, p, κ_T, α, ν and T are the density, pressure, thermal diffusivity, thermal expansion coefficient, kinematic viscosity and temperature of the fluid, respectively. A subscript 0 denotes reference quantities and $\nabla^2 = \partial^2/\partial x^2 + \partial^2/\partial z^2$. Impermeable and no-slip velocity conditions are applied at all boundaries:

$$u = w = 0 \qquad \text{at } x = 0, L, \tag{2.6}$$

$$u = w = 0 \qquad \text{at } z = 0, D. \tag{2.7}$$

https://doi.org/10.1017/S0022112004000485 Published online by Cambridge University Press

The walls and lid are assumed perfectly insulating so that:

$$\frac{\partial T}{\partial x} = 0 \qquad \text{at } x = 0, L, \tag{2.8}$$

$$\frac{\partial T}{\partial z} = 0 \qquad \text{at } z = D, \tag{2.9}$$

$$F_T = \kappa_T \rho_0 c_p \frac{\partial T}{\partial z} \qquad \text{at } z = 0, 0 < x < L/2, \tag{2.10}$$

$$T = T_c \qquad \text{at } z = 0, L/2 < x < L, \tag{2.11}$$

where c_p is the specific heat capacity. Introducing a streamfunction such that $u = \partial\psi/\partial z$ and $w = -\partial\psi/\partial x$, cross-differentiating (2.1) and (2.2), and substituting (2.5) yields the vorticity equation

$$\frac{\partial \zeta}{\partial t} + u\frac{\partial \zeta}{\partial x} + w\frac{\partial \zeta}{\partial z} = \nu\nabla^2\zeta - \alpha g\frac{\partial T}{\partial x}, \tag{2.12}$$

where $\zeta = \nabla^2\psi$ is the z-component of vorticity.

We define the dimensionless variables

$$\hat{x} = \frac{x}{L}, \quad \hat{z} = \frac{z}{D}, \quad \hat{u} = \frac{uL}{\kappa_T}, \quad \hat{w} = \frac{wL^2}{\kappa_T D}, \quad \hat{\zeta} = \frac{\zeta L D}{\kappa_T} \quad \hat{t} = \frac{t\kappa_T}{L^2}, \quad \hat{T} = \frac{T}{\Delta T}, \tag{2.13}$$

where $\hat{\zeta} = (\partial\hat{u}/\partial\hat{z}) - A^2(\partial\hat{w}/\partial\hat{x})$, and $\Delta T = F_T L/\rho_0 c_p \kappa_T$ is a scale for temperature differences based on the input flux and thermal conduction over a length L. The dimensionless vorticity and temperature equations become

$$\frac{\partial \hat{\zeta}}{\partial \hat{t}} + \hat{u}\frac{\partial \hat{\zeta}}{\partial \hat{x}} + \hat{w}\frac{\partial \hat{\zeta}}{\partial \hat{z}} = Pr\hat{\nabla}^2\hat{\zeta} - PrRa_F A\frac{\partial \hat{T}}{\partial \hat{x}} \tag{2.14}$$

and

$$\frac{\partial \hat{T}}{\partial \hat{t}} + \hat{u}\frac{\partial \hat{T}}{\partial \hat{x}} + \hat{w}\frac{\partial \hat{T}}{\partial \hat{z}} = \hat{\nabla}^2\hat{T}, \tag{2.15}$$

where

$$\hat{\nabla}^2 = \frac{\partial^2}{\partial \hat{x}^2} + \frac{1}{A^2}\frac{\partial^2}{\partial \hat{z}^2}$$

and

$$Ra_F = \frac{g\alpha F_T L^4}{\rho_0 c_p \kappa_T^2 \nu}, \quad Pr = \frac{\nu}{\kappa_T}, \quad A = \frac{D}{L}. \tag{2.16}$$

The dimensionless numbers defined in (2.16) are the flux Rayleigh number, Prandtl number and aspect ratio, respectively. In both the numerical solutions and the laboratory experiments we control Ra_F by selecting the total heat input and hence the heat flux F_T.

2.2. *Boundary-layer scaling analysis*

In a steady-state flow, vertical conduction above the cooled base is balanced by both the vertical and the horizontal advection (as these terms are of the same order in (2.15)). We assume that thermal and velocity boundary layers of the same scale thickness h are established at the base of the box (figure 1). This assumption relies on the no-slip boundary condition. We note that W. R. Young (personal communication) has shown that Rossby's scaling (along with that given here) is not expected to hold

https://doi.org/10.1017/S0022112004000485 Published online by Cambridge University Press

when convection is forced at a stress-free surface, where the momentum boundary-layer thickness scales with the depth of the box.

Using (2.3), (2.4) and taking $\partial/\partial x \ll \partial/\partial z$ (or $A^2 \ll 1$ in (2.15)), the boundary-layer balance can be expressed as

$$u \sim \frac{wL}{h} \sim \frac{\kappa_T L}{h^2}. \tag{2.17}$$

For $Pr \gg 1$, (2.12) and (2.17) lead to a balance between viscous stresses and buoyancy in the horizontal boundary-layer flow:

$$\alpha g \delta T \left(\frac{h}{L}\right) \sim \frac{\nu u}{h^2}, \tag{2.18}$$

where δT is the difference between the maximum and minimum temperatures along the length of the box given the imposed heat flux. This temperature difference is also representative of the vertical temperature difference across the boundary layer above the cooled half of the base. Conservation of heat in the boundary layer implies that

$$\rho_0 c_p \delta T u h \sim F_T L. \tag{2.19}$$

We solve (2.17), (2.18) and (2.19) to obtain the following expressions for the characteristic temperature anomaly δT, boundary-layer thickness h, boundary-layer velocity u and vertical velocity w, which in normalized form become:

$$\frac{\delta T}{\Delta T} \sim Ra_F^{-1/6}, \tag{2.20}$$

$$\frac{h}{L} \sim Ra_F^{-1/6}, \tag{2.21}$$

$$\frac{uL}{\kappa_T} \sim Ra_F^{1/3}, \tag{2.22}$$

$$\frac{wL}{\kappa_T} \sim Ra_F^{1/6}, \tag{2.23}$$

and (2.20) can be rewritten as the Nusselt number

$$Nu \sim Ra_F^{1/6}, \tag{2.24}$$

where $Nu = F_T L/\rho_0 c_p \kappa_T \delta T \equiv \Delta T/\delta T$ is the heat flux relative to that due to conduction along the length of the tank. The volume flux per unit width in the two-dimensional overturning flow scales as $V \sim uh$ and hence $V \sim \kappa_T Ra_F^{1/6}$. Note that, if we define the usual horizontal Rayleigh number as $Ra = g\alpha\delta T L^3/\nu\kappa_T$, then $Ra_F = NuRa$ and our result is the same as that obtained by Rossby (1965, 1998) for the case of convection in a square container ($A = 1$) forced by an imposed temperature difference δT (i.e. $Nu \sim Ra^{1/5}$ and $V \sim \kappa_T Ra^{1/5}$). Scaling results for other related cases are discussed in § 7.

3. Experiments

3.1. *Apparatus*

We used an acrylic tank having inner dimensions $L = 1.25$ m long, $W = 0.15$ m wide and $H = 0.2$ m deep (figure 2). In order to minimize heat loss from the tank to its surroundings, the sidewalls were double-glazed. The interior and exterior walls were 20 mm and 3 mm thick, respectively, and the 18 mm cavity between the walls was filled with argon. The sidewalls extended downwards to surround the base, heating mat and

https://doi.org/10.1017/S0022112004000485 Published online by Cambridge University Press

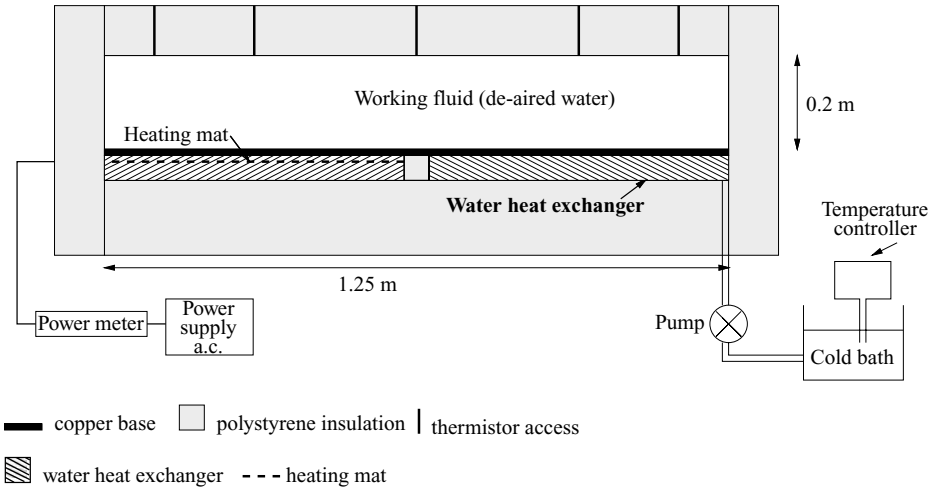


FIGURE 2. The experimental arrangement. The electric heating mat is pressed against the copper base.

heat exchanger. The entire tank was thermally insulated with expanded polystyrene foam of thicknesses 150 mm below the base, 96 mm on the endwalls, 50 mm on the sidewalls and 100 mm on the lid. The sidewall polystyrene could be removed for flow-visualization purposes.

A 10 mm thick sheet of copper formed the base of the tank. A 600 mm × 150 mm electric heating mat was clamped against the left-hand half of the copper base above a 27 mm sheet of ceramic insulation and a 20 mm sheet of acrylic, the latter bolted to the base of the walls. The heating mat provided total heat fluxes ($F_T WL/2$) between 10 and 374 W uniformly distributed over its area (i.e. $111 \leqslant F_T \leqslant 4156\ \mathrm{W\ m^{-2}}$). A 600 mm long recirculating water heat exchanger was attached beneath the other half of the base. This heat exchanger consisted of channels through which cold water was pumped from a constant temperature bath, with the recirculating water in the channels directly contacting the overlying copper base. With this design, we achieved a temperature boundary condition that was very close to uniform and constant. The coolant was held at 16 °C by a proportional controller and the upper surface of the base was close to 16.5 °C, depending only very weakly on the heat flux. A 50 mm insulating spacer between the heating mat and cold heat exchanger reduced 'short-circuiting' of heat flow directly along the copper base. A steady two-dimensional conduction solution (see Carslaw & Jaeger 1959) shows the amount of heat transported directly along the copper base is less than 0.3% of the total heat input in each experiment. Apart from the unavoidable no-slip velocity boundary condition on the two sidewalls, all boundary conditions were independent of distance across the box, thus forcing a flow as two-dimensional as possible. In a few additional runs, which we observed in only qualitative ways, the heating mat was replaced with a heat exchanger recirculating warm water, but otherwise identical to that under the cooled half of the base. The experiments were run with an imposed temperature difference (16 °C at the cool half and approximately 40 °C at the warm half).

An acrylic lid in contact with the water sealed the top of the tank. Along the lid was a series of holes with vertical tubes extending upwards through the polystyrene insulation (figure 2). Thermistor access was possible through five tubes along the centreline at $x = 0.1$, 0.3, 0.625, 0.95 and 1.15 m (measured from the left-hand endwall)

https://doi.org/10.1017/S0022112004000485 Published online by Cambridge University Press

and a second line of tubes offset 25 mm from the centreline, at $x = 0.3$, 0.625 and 0.95 m. A further three tubes at $x = 0.12$, 0.595 and 1.13 m on the centreline were used for adding dye streaks. The tubes also accommodated changes in volume of the working fluid owing to thermal expansion during the approach to thermal equilibrium.

Eight fast-response thermistors were attached to a rack which could be either traversed vertically to obtain temperature profiles at five positions along the tank or carefully positioned for simultaneous time records at eight fixed points. A traversing speed of 6.1 mm s^{-1} was used. A further two thermistors were embedded on the centreline of the copper base, close to its upper surface and 0.1 m from each endwall. The traversing mechanism and data acquisition were all controlled by computer. Time records from stationary thermistors were acquired from each sensor at approximately 0.1 samples/s and data for vertical profiles was taken at 60 samples/s. The approach to the equilibrium state was monitored with the thermistors held stationary.

3.2. *Procedure and measurements*

De-aired water was used as the working fluid to ensure that no air bubbles appeared in the tank. Once set up, the system evolved to a thermal steady state in which the convective flux leaving through the cold plate matched the imposed heat flux (less sidewall heat losses). Thus, the flux through the cooled half of the base was also imposed by the heat input flux. In some runs, the working fluid was initially at room temperature when the heating mat, cooling unit and pump were switched on. In other cases, the heating mat (or hot water heat exchanger) was switched on first in order to bring the water close to the estimated equilibrium temperature before the cooling was turned on. This latter method gave a much shorter equilibration time (~6–7 h instead of 25 h).

As an example of the equilibrated flow, a cold bath temperature of 16 °C and an input heating power of 140 W ($F_T = 1556$ W m^{-2}) led to a steady state in which temperatures in the upper three-quarters of the body of the tank were within 0.1 ° of 32.8 °C, whereas the temperatures taken from the thermistors embedded within the warm and cold ends of the copper base were 36.3 °C and 16.7 °C, respectively. The flux Rayleigh number for this case was of order 10^{14}. We note that, in this example, the range of temperatures in the flow (16–33 °C) corresponds to a thermal expansion coefficient ranging from 1.6×10^{-4} K^{-1} to 3.3×10^{-4} K^{-1} (Ruddick & Shirtcliffe 1979), a variation that has not been allowed for in the scaling analysis, but which may be significant and can be investigated using the numerical solutions. In order to minimize the fractional variation of the expansion coefficient within the tank, the cold plate temperature was set well above 10 °C. We base the Rayleigh and Prandtl numbers on the diffusivity and viscosity evaluated at the mean interior temperature of each run.

A vertical temperature profile was used to determine the thickness of the thermal boundary layer. The thermistors were traversed downwards from the lid to 1 mm above the base, with a reading every 0.1 mm. Windowed-averages based on five readings were used to reduce instrumental noise, giving a spatial resolution of ~0.5 mm. We define the boundary-layer thickness to be the height above the base at which the difference from the temperature at mid-height is 5% of the maximum temperature anomaly in that same profile. In the case of the smallest input heat power (of 10 W), an estimate for the height of the boundary layer was determined from the temperature profiles by eye.

A shadowgraph set-up was used to give qualitative images of the flow and to measure the flow velocities in the boundary layer. Potassium permanganate crystals were dropped into the tank to produce vertical dyelines. The subsequent deformation

https://doi.org/10.1017/S0022112004000485 Published online by Cambridge University Press

on the shadowgraph screen was recorded on video for later analysis. A number of frames were digitized at specified times. A comparison of frames was used to make accurate measurements of the horizontal displacement of the dyelines, and hence to determine the maximum horizontal velocity in the boundary layer. In other runs, dye tracer was released continuously from syringe tubes near the base and at either the centre or cold (right-hand) end of the box. This tracer was advected with the bottom boundary-layer flow, upwelled in the turbulent plume and travelled along the top of the tank in the plume outflow. Vertical profiles of the horizontal velocity were obtained by measuring the horizontal displacement of an initially vertical line of fine particles, released as a precipitate from a vertical length of solder wire placed in the centre of the tank (Honji, Taneda & Tatsuno 1980).

Images of the convection were also obtained using the 'synthetic schlieren' technique (Sutherland *et al.* 1999; Dalziel, Hughes & Sutherland 2000), which allowed us to classify density gradients as either stable or unstable. However, the quantitative use of this technique was limited owing to the severe refraction of light in the strong temperature gradients in the bottom boundary layer.

A calibration run was carried out to measure the heat loss coefficient from the insulated box and the heat loss (in watts) was found to be $0.7425 \times (T_{tank} - T_{lab})$. From this we infer a heat loss in all experiments of between 2 and 6% of the total flux applied to the heating mat (except for the very small input heat fluxes of 10 and 30 W, in which there was an estimated gain of 2 and 0.86 W respectively, from the surroundings). This small loss was the difference between the heat input and withdrawal fluxes. The heat gained from the room by the thin boundary layer above the cooled base ($>16\,^{\circ}\mathrm{C}$) was negligible because it intersected the walls over an area less than 4% of the surface area of the box. When the sidewall foam was removed for long periods (10–15 min), no temperature perturbation was seen in the records from the thermistors at any location in the tank.

4. Results

4.1. *Adjustment to thermal equilibrium*

The evolution of the convection to a steady state was sensitive to the initial and boundary conditions. In most runs, the whole volume of the box overturned as a single cell throughout the equilibration process. However, in experiments where the final equilibrium temperature was less than the initial temperature, a transient two-layer configuration was observed. Under these conditions there was an initial net heat loss from the tank and the cold boundary-layer water did not gain sufficient buoyancy (as it passed along the heated portion of the base) to rise as a plume to the top of the tank. Instead, it returned to the cold end at an intermediate depth above the bottom boundary layer. Two vertically stacked convection cells formed, circulating in the same rotational sense and each occupying the full length of the tank. There was a strong circulation in the lower cell, while the upper cell was much weaker, presumably driven by a small horizontal temperature gradient resulting from heat transfer between the cells.

In each case, the flow in the two-cell mode slowly evolved, with the rising plume penetrating higher until (except for the smallest heat fluxes) it eventually reached the top of the box (figure 3). We hypothesize that the evolution was governed by upward diffusion of heat through the depth of the upper cell, or at least through a thick gradient region. For a depth of order $D/2$ this implies an evolution timescale of order 1 day. Although this time is also comparable to that observed for temperature

https://doi.org/10.1017/S0022112004000485 Published online by Cambridge University Press

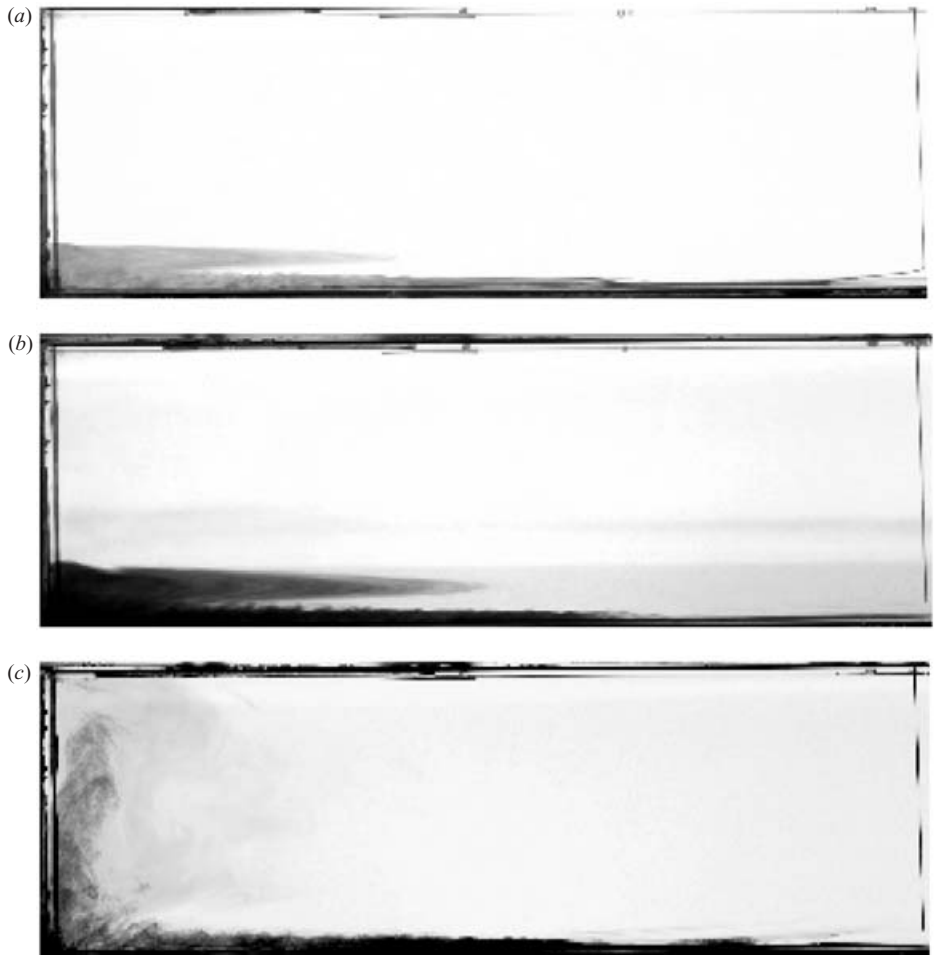


FIGURE 3. A sequence of photographs of the initial evolution in an experiment with a flux of 140 W applied to the heating mat. The initial temperature of the water was 41.5 °C. The final equilibrium temperature in the interior was 32.4 °C. Photographs show only the left-hand half of the box. The vertical tube at $x = 0.65$ m released a small amount of dye before each photograph was taken. Times of the photographs (after heating and cooling were started) are (*a*) 1 h 52 min, (*b*) 8 h 34 min, (*c*) 24 h 17 min. In (*a*), the convection was restricted to a lower region of depth 32 mm, (*b*) shows both the original dye (now light grey) which had been mixed throughout the lower cell and newly released dye which was carried by the plume to a height of 44 mm. In (*c*), the plume rises slowly through the full depth of the tank and its outflow is very broad. The flow continued to evolve until the plume was fast and narrow, and until the outflow occupied one third of the tank, as in figure 5.

equilibration in the single-cell mode of convection (§ 3.2), that time is set by the energy required to heat the whole mass of the working fluid to the final temperature, divided by the net rate of heat input (the difference between the heat input and the heat output through the cooled portion of the base). A similar diffusive adjustment was hypothesized in a related experiment (Pierce & Rhines 1996) in which a zero net buoyancy flux at the surface was achieved using salt solution and fresh-water volume sources. For the two smallest heat fluxes, the plume continued to rise through only part of the depth, and we attribute this to stabilizing effects of sidewall heat gain.

https://doi.org/10.1017/S0022112004000485 Published online by Cambridge University Press

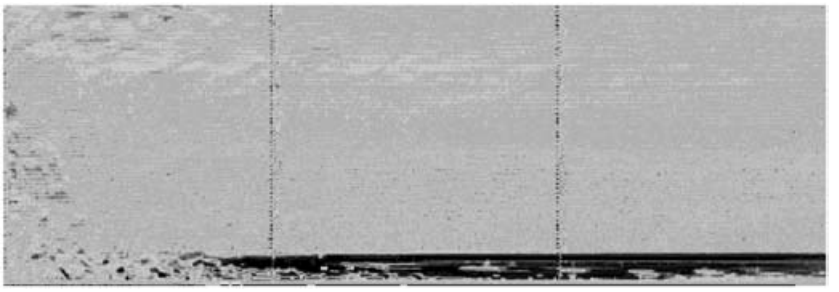


FIGURE 4. A synthetic schlieren image showing the full depth and the left-hand half of the tank over the heated base. The two vertical lines are at 200 mm intervals. The scale shows vertical refractive index gradients (light shades unstable, dark shades stable, neutral gradients in grey). Turbulent convection is seen at the left-hand end, and convection from the base erodes the stable bottom boundary layer as it flows from right to left.

The delayed equilibration due to the two-cell mode was avoided by initiating runs with colder water (usually at room temperature), so that a net heat input was required to reach the equilibrium temperature. However, our method (mentioned in § 3.2) of first heating the water using the heating part of the base, and turning on the cooling over the other half of the base shortly before the water reached the expected equilibration temperature, served well to avoid both of the slow equilibration pathways.

4.2. *The thermally equilibrated flow*

In the thermally equilibrated state, a strongly stable boundary layer covered the cooled half of the base. As this cold layer flowed across the heated half of the base, the stable temperature gradient was eroded from beneath, not by conduction but by convection driven by the bottom heating. The small-scale convection produced a mixed layer, as seen in the schlieren and dye images (figures 4 and 5). This convective vertical mixing began 50 to 100 mm from the centre of the tank and deepened with distance from the onset. The flow in all cases adjusted such that the mixed-layer thickness reached the full depth of the stable cold boundary layer within about 50 mm from the left-hand end of the box (see schlieren image, figure 4). Within about 30–50 mm from the left-hand endwall, the mixed layer fed into a narrow rising plume that hugged the endwall. Thus, the whole of the boundary layer flux first entered the mixed layer before reaching the plume.

The upwelling plume was strongly confined to the endwall, as in the experiments of Rossby (1965). The inflow to the base of the plume was characterized by small-scale convective eddies, which we expect to carry no net volume flux. Through most of its height, however, the plume exhibited turbulence as a result of a strong mean shear between the upwelling water and the relatively stationary interior. The Reynolds number in this region, based on plume width and mean vertical velocity, was around 500 for most runs. The dominant shear-generated eddies had scales comparable to the plume width, and the qualitative appearance was that of a turbulent buoyant plume (as seen in many types of experiment with a small source, except that in the horizontal convection tank a significant volume flux was present at the 'source'). These eddies were much larger than the small buoyant elements carried up from the bottom boundary layer.

At the top of the tank the outflow from the plume (figure 5) contained eddies larger than those in the plume. The perturbations of largest scale travelled slowly along the box, but were not sufficiently coherent to be tracked by eye for more than about

https://doi.org/10.1017/S0022112004000485 Published online by Cambridge University Press

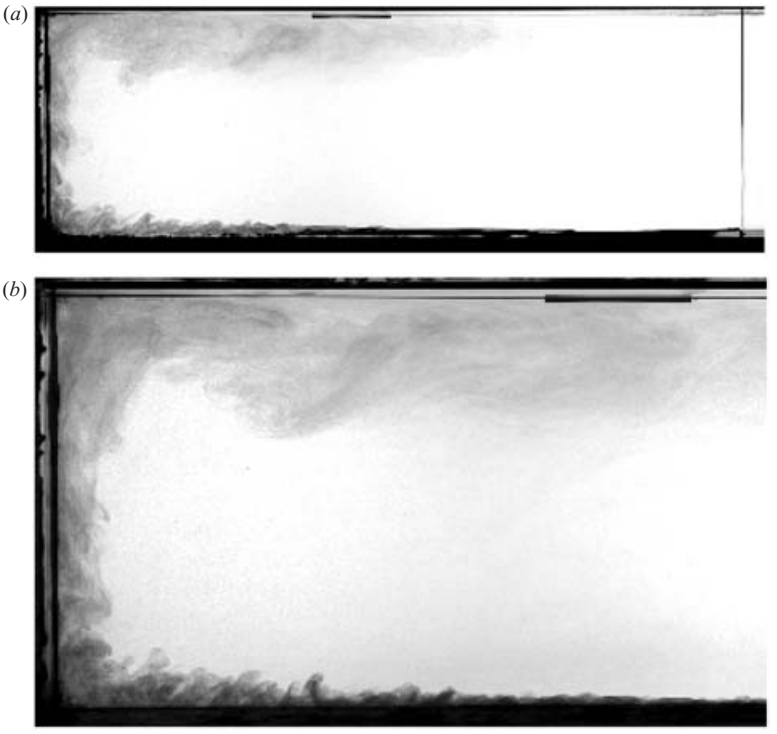


FIGURE 5. Photographs showing transport of dye tracer in an experiment with input heating power of 270 W. The vertical dye tube seen in the right-hand side of (*a*) was in the centre of the tank (at $x = 0.625$ m) and released a constant stream of dye into the bottom boundary layer. The tank was back lit with a diffusing screen placed on the far sidewall. (*a*) The left-hand half of the tank. The dye reveals vertical mixing through the depth of the convective mixed layer, penetration of the overlying stable boundary layer by the small-scale convection, shear instability in the vertical plume against the endwall, and the plume outflow at the top. (*b*) A close up of the plume and its outflow, covering approximately 35 cm of the tank from the left-hand endwall. The image in (*b*) is taken at a later time than that in (*a*). Both images show the full depth of the tank.

0.2 m. Dye tracer also revealed smaller three-dimensional motions in this region. The outflow immediately adjacent to the plume occupied approximately a fifth of the box height D, but within 0.1 to 0.2 m of the endwall the outflow (measured from either horizontal velocity or tracer) thickened to a depth of approximately $D/3$. This remained uniform along the remainder of the length of the box. Downwelling motion in the interior was very slow, and was difficult to measure in the presence of the eddying and apparently weakly turbulent horizontal flow. After long periods of continuous tracer release, the dye tracer showed downward mixing, and revealed a region of stronger downwelling at the far end of the box. The tracer also showed a tendency to avoid accumulation near the mid-depth line in the interior at large times. Tracer was recycled toward and into the upwelling plume at depths above the boundary layer. Eventually, the dye also entered the boundary layer and was recycled through the plume. These observations imply the presence of turbulent entrainment into the plume through at least the lower half of the box depth.

Closer examination of the small-scale convection at the base (including viewing from above) revealed coherent rolls aligned with the boundary-layer flow for a short distance (about 50 mm) along the heated base, beginning 50 to 100 mm from the centre

https://doi.org/10.1017/S0022112004000485 Published online by Cambridge University Press

of the box. Similar streamwise convection rolls have been observed in experiments with shear flow in a sloping plane layer with a heated base (Hart 1971) (though in that case there was no stable overlying density gradient as encountered in the present flow). Such rolls will not be captured in two-dimensional numerical solutions (see § 6), where the flow is assumed independent of the cross-stream direction. They are also not visible to optical methods that integrate refractive index variations along light paths through the width of the tank. The rolls were short and gave way to fully three-dimensional convection. Over most of the heated base the small-scale convection had a turbulent appearance and consisted of small plumes and eddies that penetrated a short distance into the overlying stable gradient of the boundary layer before rebounding. As best we could determine, the vertical profile of horizontal velocity within the turbulent mixed layer indicated zero mean shear. Between 50 and 100 mm from the left-hand endwall, the small-scale mixing penetrated to the full depth of the boundary layer before being swept upward with the mean flow in the larger ascending plume.

The shadowgraph and dye tracer observations for runs with an imposed temperature difference showed no obvious difference in circulation pattern or flow details, apart from an onset of small-scale convection in the boundary layer a few centimetres closer to the centre of the box. This system too was left to reach a state of zero net heat flux, and the difference between the cases of imposed flux and imposed temperature difference is only that in one case the input flux was spatially uniform, whereas in the other the boundary temperature of the heated portion of the base was uniform.

4.3. *Temperature profiles and Rayleigh-number dependence*

Typical vertical temperature profiles under equilibrated conditions for three different input heat fluxes are shown in figure 6. Above the thermal boundary layer, the interior fluid was close to isothermal. The boundary layer was of remarkably uniform thickness along the whole length of the tank (except close to the left-hand endwall). The horizontal temperature gradient was weak within the boundary layer along the length of the cold plate, large in the lower (heated) portion of the boundary layer over the heated base between $x = L/4$ and $L/2$, and again quite small within the warm convective mixed layer at $x < L/4$. The existence of the convective mixed layer is evident from the temperature records, since the profiles at $x = 0.1$ and 0.3 m above the hot plate show a region of unstable temperature gradient (these measurements are not averaged over time), and the unstable region deepens towards the left-hand endwall. The highest temperature measured in the boundary layer (at the lowest measurement point, 1 mm above the base, and $x = 0.1$ m) was very close to – but, importantly, slightly greater than – the average interior temperature: for example, with heat input of 140 W, an estimate of the temperature excess providing buoyancy to the upwelling plume (as measured by the temperature inversion in the profile of figure 6*a*) was 0.34 °C. The plume outflow at the top of the box had a small thermal signature (a temperature excess $\leqslant 0.1$ °C throughout the top 40–50 mm). This signal decreased with distance along the box. For most of the depth of the box (between $z = 30$ and 180 mm) the vertical temperature gradients were extremely small (of order 0.1 °C over 150 mm).

At larger Rayleigh numbers (achieved by increasing the power supplied to the heating mat), the overall thicknesses of the thermal boundary layer and the bottom convective layer were smaller, the circulation was stronger and there were larger temperature differences and velocities in the boundary layer. For the purpose of calculating the Nusselt number (2.24) for each experiment, δT was defined as the

https://doi.org/10.1017/S0022112004000485 Published online by Cambridge University Press

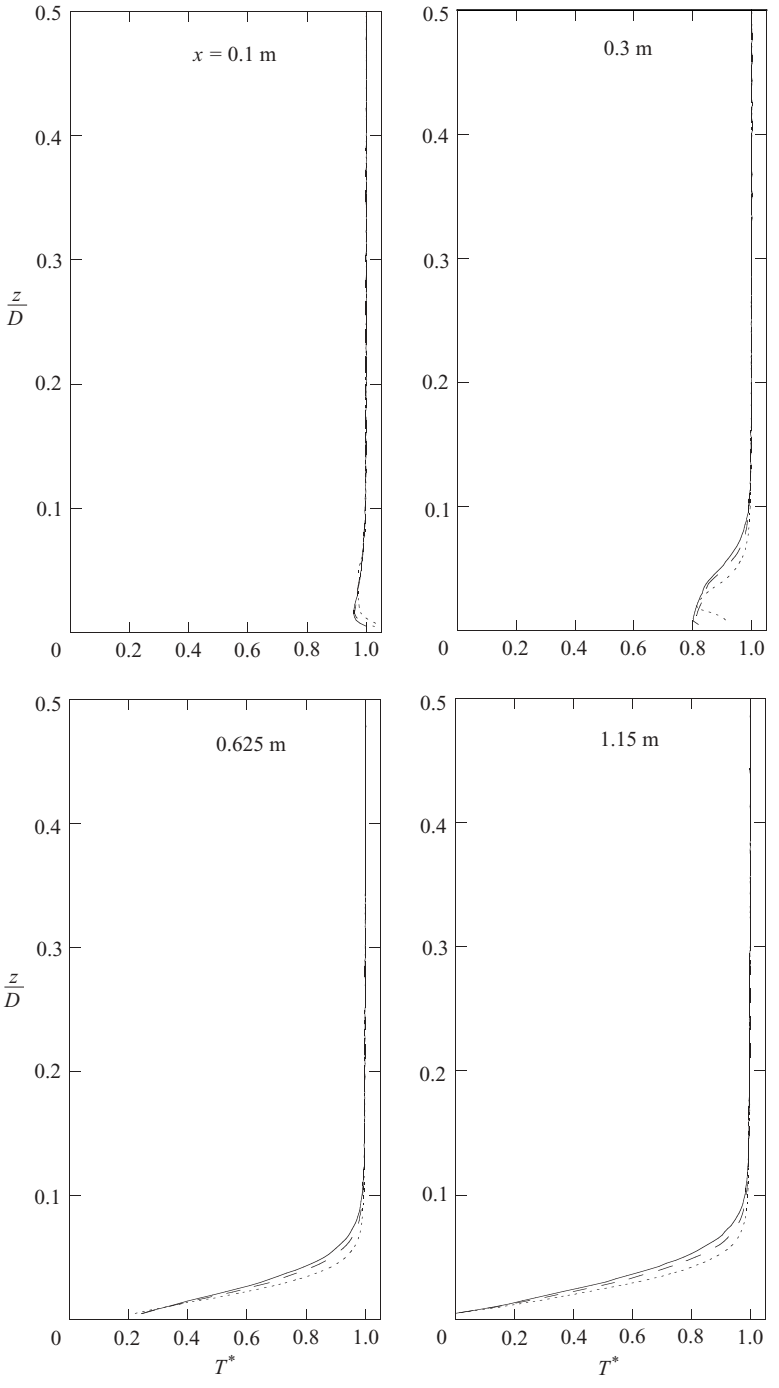


FIGURE 6. Profiles of the normalized temperature T^* through the boundary layer at $x = 0.1$, 0.3, 0.625 and 1.15 m, where $T^* = (T - T_{ref})/(T_{int} - T_{ref})$, T_{ref} is measured at $x = 1.15$ m and 1 mm above the base for each heat flux, and T_{int} is the temperature at mid-depth for each profile. The solid line, dashed line and dotted line are from experiments with input heat fluxes of 100, 140 and 271 W, and corresponding Ra_F of 1.05×10^{14}, 1.75×10^{14} and 4.57×10^{14}, respectively. Note that the vertical axis corresponds to only half the box depth.

https://doi.org/10.1017/S0022112004000485 Published online by Cambridge University Press

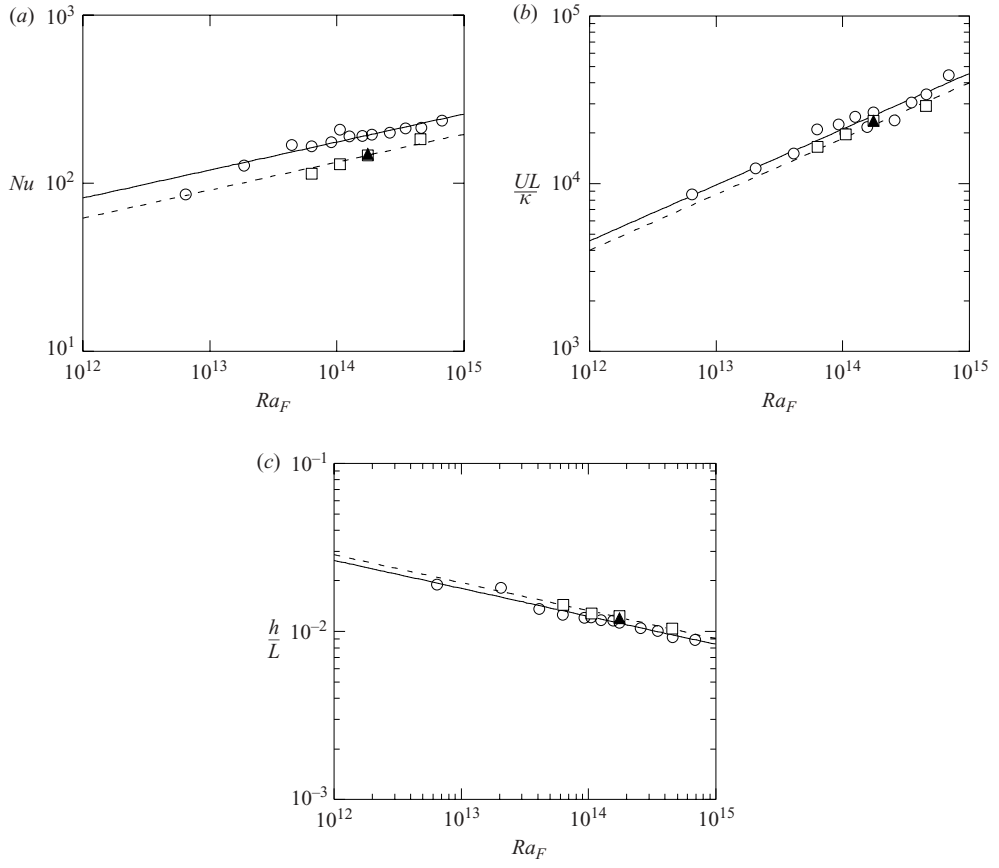


FIGURE 7. (*a*) Normalized heat flux Nu, (*b*) boundary layer velocity UL/κ, and (*c*) boundary layer thickness h/L plotted as functions of Ra_F. The solid and dashed lines are best fits of the predicted power laws (2.24, 2.22 and 2.21) to the laboratory data (○) and numerical data (□), respectively. The solid lines are $Nu = 0.81587Ra_F^{1/6}$, $UL/\kappa = 0.45525Ra_F^{1/3}$ and $h/L = 2.649Ra_F^{-1/6}$. The laboratory data point with lowest Rayleigh number corresponds to a heat input of 10 W and has a much greater uncertainty than the other data. Results from the numerical solutions □ are also shown. The result from the additional numerical run using a temperature dependent expansion coefficient is shown by ▲.

temperature difference between $x = 0.1$ and 1.15 m at a height 1 mm above the base. The temperature profiles were used to estimate the boundary-layer thickness h in (2.21) and dye streaks were used to measure the maximum velocity u for (2.22).

When making a comparison between the data and the scaling theory, the relevant molecular quantities are those for water. These properties were evaluated at the mean temperature of the interior region of the circulation. When cast in dimensionless form, the measurements agree well with the scaling analysis (figure 7).

5. A model for the convective mixed layer

The convective mixed layer (CML) above the heated half of the base is embedded within an otherwise stable temperature gradient established by conduction (figure 8). This part of the flow was steady on long timescales, with variability confined to the time and length scales (∼10 s, ∼10 mm) of the small cells, plumes and eddies that

https://doi.org/10.1017/S0022112004000485 Published online by Cambridge University Press

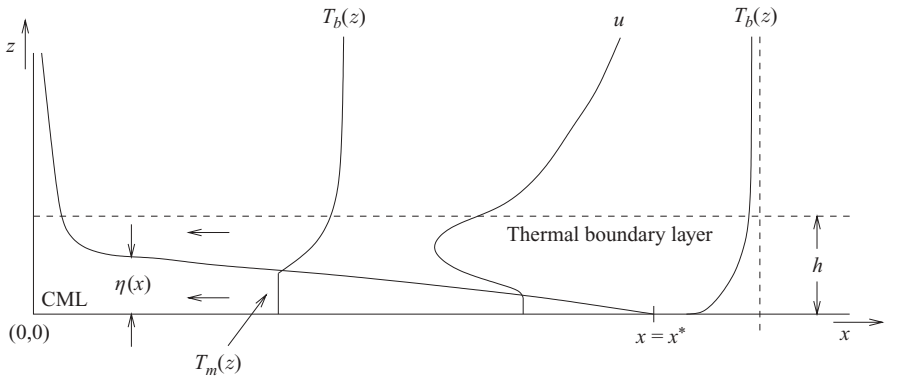


FIGURE 8. The convective mixed layer. The vertical scale is exaggerated.

were identified in the CML and the (somewhat larger) eddy time and length scales ($\sim$100 s, $\sim$30–100 mm) in the upwelling endwall plume and plume outflow region.

A simple theoretical description of the CML is instructive. We denote the height of the CML by η (figure 8) and make the following assumptions:

(i) The boundary layer is very thin compared to its length and everywhere slowly varying in the horizontal;

(ii) $\eta = 0$ at $x = x^* \leqslant L/2$ and $\eta \to D$ at $x = 0$, where x^* is the position at which instability first occurs, potentially estimated from a local Rayleigh number criterion;

(iii) The horizontal velocity within the boundary layer can be characterized by $\bar{u}$, a velocity averaged over the CML in both x and z (the vanishing velocity at the left-hand endwall is not included in this calculation);

(iv) The CML is vertically well mixed so that its temperature T_m is a function of x alone;

(v) The CML deepens only by 'encroachment' due to warming and not due to inertial entrainment processes (i.e. there is a continuous density profile, with no density step or inversion; Manins & Turner 1978);

(vi) Heat conduction from the convecting layer into the overlying stable region can be neglected;

(vii) The temperature distribution in the stable cold boundary layer (outside the CML) is established over the cooling half of the base before being advected to the left, and can be described by a simple analytic expression, $T_b(z)$ (given below) for $z > \eta(x)$.

An approximation for the outer stable temperature profile is found using the steady form of the advection–diffusion equation (2.4) with $\partial/\partial x \ll \partial/\partial z$ (or from (2.15) with $A \ll 1$):

$$\bar{u}\frac{\partial T_b}{\partial x} + w\frac{\partial T_b}{\partial z} = \kappa_T \frac{\partial^2 T_b}{\partial z^2}, \tag{5.1}$$

where boundary conditions are

$$T_b(z) = T_0 \qquad \text{as } z \to \infty, \tag{5.2}$$

$$T_b(z) = T_c \qquad \text{at } z = 0. \tag{5.3}$$

In order to find a highly idealized, horizontally uniform solution in a thin boundary layer above the cold plate (as in the thermocline solution given by Pedlosky 1979, chap. 6), we set $\partial T/\partial x = 0$ everywhere in (5.1). This is the vertical balance previously

https://doi.org/10.1017/S0022112004000485 Published online by Cambridge University Press

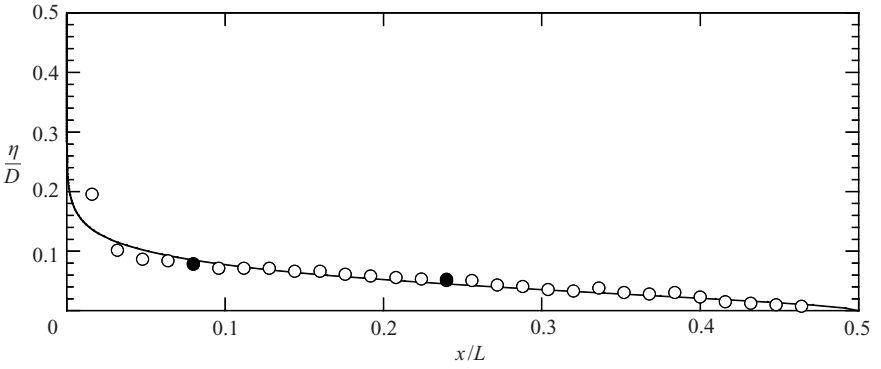


FIGURE 9. Normalized depth, η/D, of the convective mixed layer over the heated half of the base, as a function of horizontal distance from the left-hand endwall for input heat flux 140 W. ○, measured depth from shadowgraph; ●, depth estimated from measured temperature profiles; —, mixed layer model (5.8) using a stable boundary layer of height $h = 5.2$ mm. Note that the vertical axis corresponds to only half of the depth, and that the flow is towards decreasing x.

expressed in (2.17), where the assumption is that most of the heat carried downward to the boundary by vertical advection is removed by conduction. The solution is

$$T_b(z) = T_0 - \delta T \exp\left(\frac{-z}{h}\right), \tag{5.4}$$

where $\delta T = T_0 - T_c$ and $h = -\kappa_T/w$. Conservation of heat in the horizontal flow over the heating plate leads to the integral constraint,

$$\int_0^\eta [T_m(x) - T_c]\,\mathrm{d}z - \int_0^\eta [T_b(z) - T_c]\,\mathrm{d}z = \frac{F_T}{\rho c_p}\frac{(x - x^*)}{\bar{u}}. \tag{5.5}$$

Substitution of (5.4) into (5.5) and integration over the depth of the CML gives

$$\eta T_m(x) - \eta T_0 - h\delta T \exp\left(\frac{-\eta}{h}\right) + h\delta T = \frac{F_T}{\rho c_p}\frac{(x - x^*)}{\bar{u}}. \tag{5.6}$$

Continuity of temperature and density at the top of the CML, at $z = \eta$, (which follows from the 'encroachment' assumption) imply

$$T_m = T_b(\eta) = T_0 - \delta T \exp\left(\frac{-\eta}{h}\right). \tag{5.7}$$

Substitution into (5.6), and making use of our previous scaling for δT, h and $\bar{u}$ ((2.20)–(2.22)), yields

$$k\frac{(x - x^*)}{L} = 1 - \left(1 + \frac{\eta}{h}\right)\exp\left(\frac{-\eta}{h}\right), \tag{5.8}$$

where k is a constant of order one that is evaluated by applying the condition $\eta = D$ at $x = 0$ (thus assuming that the mixing penetrates the full depth of the box only at the end and not at larger values of x).

The solution (5.8) for the CML height is shown in figure 9 for the case $x^* = L/2$ and $h = 5.2$ mm (as appropriate for $Ra_F = 1.55 \times 10^{14}$), where it is compared with the height measured from the shadowgraph. From $x/L = 0.5$ to $x/L \approx 0.3$, the rate of convective layer deepening decreases with distance from the onset of small-scale convection at x^*. This reflects the uniform boundary heat flux being mixed into a

https://doi.org/10.1017/S0022112004000485 Published online by Cambridge University Press

deepening layer. The rate of deepening with distance increases again closer to the endwall, where the CML is encroaching into a much smaller overlying density gradient at the top of the conductive stable boundary layer. The solution (despite the highly simplified formulation of the problem) adequately describes the shape of the CML and the way in which the mixing rapidly deepens close to the end of the box. We conclude that the near-steady large-scale horizontal flow suppresses convective instability in the region of destabilizing buoyancy flux through advection of the stable boundary-layer density stratification, from the region of stabilizing buoyancy flux.

6. Numerical solutions

6.1. *Solution methods*

The governing equations (2.1)–(2.5) were solved numerically using the CFD package FLUENT (version 6.1), which employs a finite-volume method. We used the two-dimensional implicit segregated solver (with the PRESTO! interpolation scheme for pressure, the PISO algorithm for pressure–velocity coupling and the QUICK scheme for discretization of the momentum and energy equations). This discretization scheme is third-order and provides a robust solver that reduces artificial numerical diffusion (Leonard 1984). The solver is non-hydrostatic and we do not use a turbulence closure model for sub-gridscale processes. This is in contrast to most ocean GCMs, which typically use a hydrostatic approximation and parameterize the convective processes by a 'convective adjustment' scheme (e.g. Winton 1995). In order to verify the suitability and accuracy of the schemes for our problem, we first repeated the numerical experiments with convection in a square box reported by Rossby (1998). In these verification runs, the grid spacing used was similar to that employed in the original work. Viscosity and diffusivity were varied (because FLUENT solves the governing equations in dimensional form) to reproduce $Pr = 10$ and Rayleigh numbers across the range $10^3 < Ra < 10^8$. When re-cast in dimensionless form, the results were in excellent agreement with those obtained by Rossby (1998).

The grid used for solutions with the smaller aspect ratio and larger Rayleigh numbers of our experiments consisted of a coarse array of 10 mm × 10 mm cells in the interior and a fine boundary-layer mesh in regions with small-scale activity or large temperature gradients. The boundary-layer meshes along the lid and base were identical and consisted of 12 rows each. The row adjacent to each boundary had cells of height 0.5 mm and the cell height increased by a factor of 1.3 for each row further from the boundary, giving an overall boundary-layer mesh of height 37.2 mm. On the sidewall at the heated end of the tank there was a boundary-layer mesh 3 cells (approximately 20 mm) wide. The no-slip condition was applied on all boundaries and there was no heat flux through the endwalls or the lid. This two-dimensional solution does not allow for heat loss or no-slip conditions at the long (front and back) sidewalls. Water properties were generally set as constants and evaluated at the mean interior temperature at thermal equilibrium in the equivalent laboratory experiments. The heat fluxes and water properties used are shown in table 1.

Runs were carried out with four different fluxes applied to the heating boundary ($0 < x < 0.6$ m), $F_T = 778, 1111, 1556$ and $3000\,\mathrm{W\,m^{-2}}$, and the temperature on the cold boundary ($0.65 < x < 1.25$ m) was set to 16 °C. For runs 1 and 2 the working fluid was initially at 20 °C and there was no motion in the interior. Runs 3 and 4 were initialized with the converged solution from the next smaller heat flux (runs 2 and 3, respectively). The solution was advanced in time using a second-order time-stepping scheme until convergence was obtained. The solution convergence was monitored

https://doi.org/10.1017/S0022112004000485 Published online by Cambridge University Press

Run	F_T (W m^{-2})	$\alpha(\times10^{-4})$ (K^{-1})	ρ_0 (kg m^{-3})	$\kappa_T(\times10^{-7})$ (m^2 s^{-1})	c_p (J kg^{-1} K^{-1})	$\nu(\times10^{-7})$ (m^2 s^{-1})
1	778	2.5954	996.95	1.438	4178.7	8.836
2	1111	2.8932	996.11	1.452	4178.0	8.258
3	1556	3.2394	994.94	1.474	4177.6	7.627
4	3000	3.8220	990.58	1.544	4178.6	6.109

TABLE 1. Values of heat fluxes and water properties used in the numerical experiments with constant molecular properties. Properties derived from Ruddick & Shirtcliffe (1979) and polynomial interpolation of values given in Batchelor (1967, Appendix 1).

using a time series of the average temperature in the tank and also the total heat flux leaving through the cooled plate. The solution was judged to have reached thermal equilibrium when the net heat flux into the tank was less than 3% of the heat flux applied to the heating boundary, i.e.

$$\int_{0.65}^{1.25} \kappa_T\, \rho_0\, c_p \left.\frac{\partial T}{\partial y}\right|_{y=0} \mathrm{d}x \geqslant 0.97 \times (0.6 \times F_T).$$

Time steps were sufficiently small such that the Courant–Friedrichs–Lewy condition for numerical stability was satisfied. Runs 1 and 2 used an initial time step of 1 s and this was halved as velocities increased. In runs 3 and 4 a time step of 0.25 s was used throughout the evolution. After the solution reached thermal equilibrium, the unsteady formulation of the problem revealed short-period fluctuations in the flow.

In order to examine the solution dependence on the grid spacing, the mesh was refined using a hanging node algorithm (which splits each rectangular grid cell into four equal area cells). The computational time for convergence became extremely large with the finer mesh. However, the solutions were very similar to those obtained on the standard grid, although the refined grid solutions showed more structure in the unsteady small-scale convection 'rolls' over the heated base and in the eddying motions in the plume.

6.2. *Solutions*

The two-dimensional numerical solutions show excellent agreement with the laboratory observations. Figure 10 shows an instantaneous solution from run 3, while figure 11 shows the mean flow and temperature fields. The mean fields were formed by averaging 720 solutions taken at 5 s intervals over a 1 h period. Vertical profiles of the horizontal velocity are shown in figure 12 where the profiles at the left and centre are compared with the measured profiles from laboratory experiments. In a region near the plume, the horizontal velocity (figures 10*a* and 11*a*) is directed away from the plume throughout the top third of the box. Below this, the flow is mainly to the left (into the plume), relatively slowly in the interior and much faster in the boundary layer (the bottom 25 mm). There is a small mean flow away from the plume immediately above the boundary layer (figures 10*a* and 11*a*), possibly indicating that a thin uppermost part of the stratified boundary-layer flow toward the plume is turned back to the right instead of entering the plume. Horizontal velocities of both signs generally increase with proximity to the left-hand end of the box. There is a weak enhancement of the downwelling velocity at the far end of the box. The temperature gradient in the interior (figure 10*d*) is small but positive (a variation of 0.12 °C over

https://doi.org/10.1017/S0022112004000485 Published online by Cambridge University Press

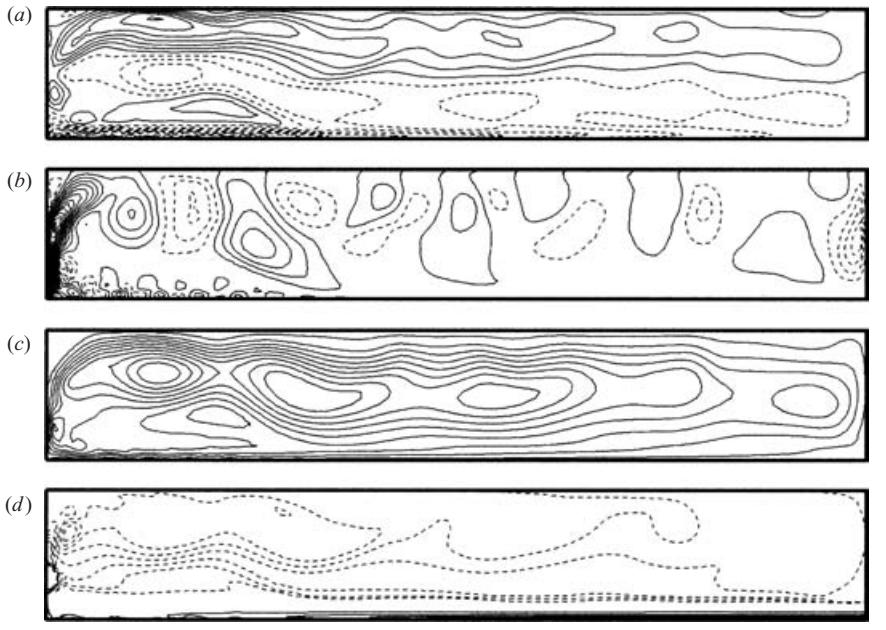


FIGURE 10. A snapshot in time of the numerical solution for run 3 (see table 1) with a total applied heat flux of 1556 W m^{-2} and cold plate temperature of 16 °C. This run is equivalent to the laboratory experiments with power 140 W applied to the heating mat. Contours of: (*a*) horizontal velocity u, (*b*) vertical velocity v, (*c*) streamfunction ψ and (*d*) temperature T. In (*a*) and (*b*), solid lines show positive and zero velocities, dashed lines are negative velocities. The contour interval is 0.6 mm s^{-1} in (*a*), 0.3 mm s^{-1} in (*b*) and 0.015 kg s^{-1} in (*c*). In (*d*), the solid lines are contours with interval 3 °C and the dashed lines are the 0.01 °C contours between 38.85 and 38.95 °C.

the upper three-quarters of the depth). These results confirm significant entrainment into the plume from above the boundary layer, despite the two-dimensional constraint.

There is a substantial degree of unsteadiness in the flow details in figure 10, and even the 1-hour average (figure 11) still shows some small unsteadiness in parts of the plume outflow where the vertical velocity is directed upward (marked by the contour closest to the centre of the box). In the interior of the box, the solutions show a series of large disturbances, causing alternating upward and downward velocities superimposed on a small mean downwelling flow (figure 10*b*). Referring back to the experimental observations of overturning eddies and mixing, we conclude that these structures are more eddy-like than wave-like. An animation of the solution shows the eddies moving to the right and decaying in amplitude. In run 3, there are typically six eddies, approximately equally spaced along the length of the box, and each eddy takes approximately 1200 s to travel from the heated end to the cooled end.

Above the heated boundary, the two-dimensional solution contains a regular set of perturbations having small length scales. We interpret these as convection 'rolls' (which in the two-dimensional solution must be aligned in the cross-stream direction, hence in the direction normal to the rolls observed in the experiments). The rolls are characterized by a positive correlation between the temperatures and vertical velocity component. The height to which the perturbations extend increases towards the left-hand end of the box. The variation in horizontal velocity through the boundary layer also indicates a shear that will cause the rolls to rotate in an anticlockwise direction

https://doi.org/10.1017/S0022112004000485 Published online by Cambridge University Press

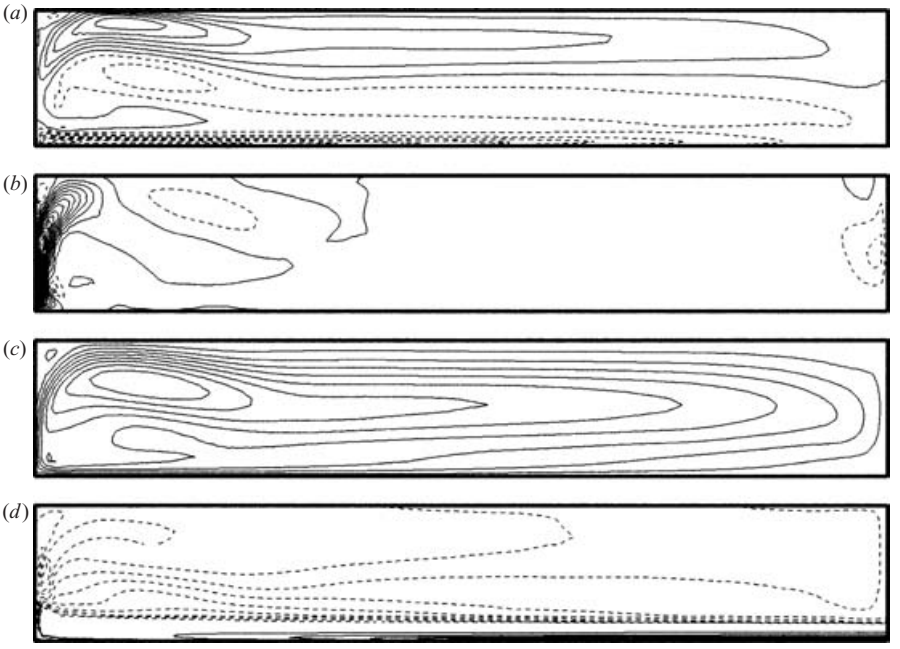


FIGURE 11. Time-averaged flow and temperature fields for the same run as figure 10 (run 3, table 1). Contours of: (*a*) horizontal velocity u, (*b*) vertical velocity v, (*c*) streamfunction ψ and (*d*) temperature T. The contour intervals are the same as in figure 10.

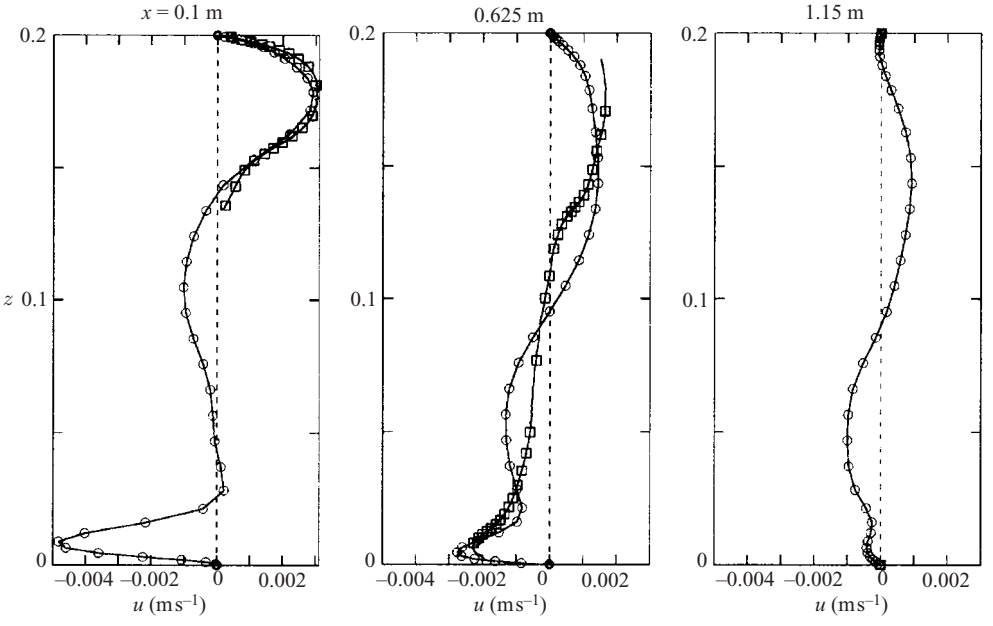


FIGURE 12. Vertical profiles of horizontal velocity: ○, numerical results; □, corresponding laboratory measurements. The dashed vertical lines show the zero velocity reference line for each position. Laboratory results for the leftmost ($z < 0.13$ m) and rightmost profiles are not included as accurate measurements were particularly difficult to obtain in these regions.

https://doi.org/10.1017/S0022112004000485 Published online by Cambridge University Press

while they are being advected to the left. The scale of the convection rolls was dependent upon the cell size, with finer meshes giving a larger number of narrower and taller rolls. However, the large computational time required for convergence with finer meshes makes a full study of this effect impractical. In any case, the two-dimensionality of the solution is unrealistic in this region of the flow. The rolls disappear altogether in the time-averaged solution. When animated, the solutions also show these rolls forming coherent parcels of warm water that move upward in the upwelling plume. These are characterized by a timescale much smaller than that of the larger eddies in the outflow.

The flux Rayleigh number, Nusselt number, boundary-layer thickness and boundary-layer velocity for the computed solutions are included in figure 7 for comparison with the laboratory results. The values were calculated in a manner similar to that used for the laboratory experiments (§ 3.2). The Nusselt number was based on the temperature difference between the nodes closest to $(x, y) = (0.1, 0.001)$ m and $(1.15, 0.001)$ m. For the boundary-layer velocity, we use the maximum horizontal velocity close to the centre of the box ($x = 0.62$ m). The top of the thermal boundary layer generally lay between two nodes in the vertical, and a linear interpolation between these nodes was used to estimate the thickness. The results agree well with the scaling laws computed in § 2.2.

Nusselt numbers for the numerical solutions are approximately 25–40% lower than the laboratory values, reflecting greater temperature differences δT in the former. This difference may be a result of the unrealistic rendition of the three-dimensional small-scale convection in the boundary layer (less vigorous convection, leading to a larger temperature difference for the applied heat flux) or the imperfect wall insulation in the laboratory. If the Nusselt number is calculated using the maximum temperature difference along the base in the numerical solutions (i.e. between $x = 0$ and $x = 1.25$ m), the Nusselt number is further decreased by up to 25%.

When our results are cast in the form $Nu = CRa^{1/5}$, the value of the constant C for the fit to the numerical data (using the maximum temperature difference along the base for δT) is 0.41. This is similar to, but slightly greater than, the value of 0.35 obtained by Rossby, indicating that the results are not sensitive to aspect ratio and bottom boundary conditions. The value of the constant from the fit to our experimental data is 0.78 which is a factor of 2 larger than the experimental value ($C = 0.4$) obtained by Rossby. We expect that the greater values for the constants in our study are due largely to the convective mixing near the boundary, but note that our experimental value will be larger owing in part to the measurement of δt between locations 0.1 m from the ends of the tank.

In one additional run, we used an accurate representation of the nonlinear equation of state for freshwater, which gives an increase in the expansion coefficient with increasing temperature, as expected in the laboratory experiment. Characteristics of the solution are plotted in figure 7 and are similar to the previous results. Likewise contour plots of temperature, streamfunction and velocity components show no significant difference from those in figure 10.

7. Discussion and conclusions

The circulation forced by differential heating of a horizontal boundary at smaller aspect ratios and larger Rayleigh numbers than previously available remains highly asymmetric. The flow is characterized by a tightly confined plume at one end of the box, broadly distributed vertical advection in the interior, and enhanced return flow

https://doi.org/10.1017/S0022112004000485 Published online by Cambridge University Press

against the opposite endwall. A stably stratified thermal boundary layer is maintained by diffusion over the region of stabilizing boundary flux, and buoyancy forces a flow along the boundary toward the region of destabilizing boundary flux. This advection of stratification tends to suppress convective instability. Both laboratory measurements and numerical solutions confirm the validity of buoyancy–viscous scaling laws for the dimensionless heat flux, the boundary-layer thickness and horizontal velocities in the equilibrium flow (with no-slip boundaries). Hence, the heat flux and the diffusivity in the boundary layer govern the rate of overturning. The volume flux per unit width through the boundary layer is $V \sim 0.87(\kappa_T L)^{2/3}(g\alpha F_T/\rho_0 c_p \nu)^{1/6}$ and the temperature difference required to accommodate the heat flux is $\delta T \sim 1.2\kappa_T^{-2/3}(\nu/g\alpha)^{1/6} L^{1/3}(F_T/\rho_0 c_p)^{5/6}$. (These compare with $V \sim \kappa_T^{4/5}\nu\delta T^{1/5}$ and $F_T \sim \kappa_T^{4/5}\nu^{-1/5}\delta T^{6/5}$, where we omit other variables, for the case of an imposed temperature difference; Rossby 1965, 1998.)

In transient cases, irrespective of the initial conditions, the flow evolves toward an equilibrium state in which the plume retains just enough buoyancy to carry away from the forcing boundary all of the mass flux driven along the horizontal boundary layer, as required by continuity. The transient flow also involves a diffusive adjustment (if required) far from the forcing boundary, which ensures that the plume eventually penetrates through the full depth of the box.

In the experiments, the expansion coefficient of water varies with temperature and, although the net boundary heat flux is zero, buoyancy is not conserved and the cooling and heating buoyancy fluxes are not equal. However, the numerical solutions with a constant or variable thermal expansion coefficient indicate that the variable expansion coefficient has no significant effects. In all cases, once in equilibrium, there is zero net heat flux into the box. The flow appears to be insensitive to the bottom thermal boundary conditions (of flux or temperature, or piecewise or linear variation).

The turbulent vertical plume carries water through the depth of the box, entraining interior water, and maintaining a small but dynamically important vertical temperature gradient in the box interior. Similar entrainment and recirculation in the interior was observed in the solutal buoyancy experiments of Pierce & Rhines (1996, 1997). The eddying behaviour in the unsteady plume outflow involved periodic eddy formation a short distance away from the plume and on a timescale much longer than that of the eddies in the plume. This contrasts with the case computed by Paparella & Young (2002), where eddies were formed in the plume (in that case located in the centre of the box) before they were carried away in the outflow.

Another new observation is the region of small-scale three-dimensional thermal convection embedded within the otherwise stable thermal boundary layer of the overturning circulation. This convection forms a mixed layer (the CML) over the region of destabilizing boundary forcing. A convectively unstable boundary layer also exists in our numerical solutions, but these solutions allow only two-dimensional rolls aligned across the mean flow. The CML deepens with distance from the onset of small-scale convection in a manner consistent with encroachment into the overlying gradient as a result of warming (the physical equivalent of 'convective adjustment' in GCMs). The horizontal mass flux in the CML feeds directly into, and becomes, the vertical plume against the endwall. For each applied heat flux, the system adjusts so that vertical mixing breaks through the thermocline only at the end of the box. The full horizontal volume flux carried in the thermocline and plume passes through the mixed layer close to the end of the box. The plume location can be altered by a sufficiently large extremum in boundary temperature or heat flux remote from the endwalls (Pierce & Rhines 1996; Paparella & Young 2002).

https://doi.org/10.1017/S0022112004000485 Published online by Cambridge University Press

The result that a deep and turbulent overturning (rather than a shallow and creeping flow) can be generated and maintained by thermal forcing at the surface is at odds with some interpretations of Sandström's theorem (see Jeffreys 1925; Huang 1999). However, the theorem actually says nothing about the kinetic energy (or the stability) of the flow. This theorem neglects diffusion and the flow is therefore described by the theoretical prediction for the volume-averaged rate of viscous dissipation (equation (1.1); Paparella & Young 2002) in the limit of vanishing diffusivity (i.e. $\overline{\epsilon} \to 0$). Evaluation of the identity (1.1) for the actual laboratory conditions is straightforward. In the experiments with heat flux $F_T = 1556\,\mathrm{W\,m^{-2}}$, the horizontally averaged temperature was 32.4 °C at the top and 21 °C at the base. Taking the interior (maximum) value of the expansion coefficient $\alpha = 3.3 \times 10^{-4}\,\mathrm{K^{-1}}$, the molecular thermal diffusivity $\kappa = \kappa_T = 1.4 \times 10^{-7}\,\mathrm{m^2\,s^{-1}}$ and $g = 9.8\,\mathrm{m^2\,s^{-1}}$, the box-averaged dissipation per unit mass becomes $\overline{\epsilon} = 2.6 \times 10^{-8}\,\mathrm{m^2\,s^{-3}}$. Taken on its own, this value may appear to be very small. We ask, however, whether the energy supplied by the buoyancy flux can sustain mechanical mixing in the interior. The vigour of turbulent mixing in a stratified fluid is measured by the quantity $\epsilon/\nu N_i^2$, where $N_i = [(-g/\rho_0)\,\partial\rho/\partial z]^{1/2}$ is the local buoyancy frequency: values greater than 10 imply weak turbulent mixing whereas values greater than 10^3 indicate strong turbulence (Barry *et al.* 2001). For values less that order 1, mixing is expected to become increasingly intermittent. The interior temperature gradient of 0.12 °C over 0.15 m gives $N_i = 5.1 \times 10^{-2}\,\mathrm{s^{-1}}$. Taking the viscosity of water at the interior temperature $\nu = 7.8 \times 10^{-7}\,\mathrm{m^2\,s^{-1}}$ and the average dissipation rate from above gives $\overline{\epsilon}/\nu N_i^2 = 13$. The local dissipation rate ϵ need not be uniform. However, we have no further information on its spatial variability other than the expectation that it is largest in the plume. Hence, we conclude by observation that the above average value admits conditions of 'weak' mixing in interior flow in horizontal convection. Our qualitative observations of tracer behaviour indicate mixing much greater than could be achieved by molecular diffusion.

In considering the relevance of the buoyancy-driven flow to the meridional overturning circulation of the oceans (the MOC), we first recall the absence in the computations and experiments of geostrophic balance, mean flows due to surface wind stress, internal mixing by wind and tides. Hence, the model is governed by a buoyancy–friction balance in the boundary layer, the largest scales are two-dimensional, and there is no wind stress or vertical Ekman pumping. In contrast, the MOC is likely to be described by geostrophic scaling (Bryan & Cox 1967; Park & Whitehead 1999; Park & Bryan 2000), the flow is three-dimensional and the upper boundary layer may be strongly influenced by effects of wind stress. Despite these differences, however, the non-rotating convection can instruct us on some of the fundamental dynamics of the zonally averaged overturning in a closed single hemisphere ocean basin. Effects of rotation are not important in a first approximation because lateral transport in the deep ocean interior is rapid compared to vertical transport (Munk & Wunsch 1998). The stably stratified bottom thermal boundary layer in the experiments is analogous to the ocean thermocline, the vertical plume represents the deep downwelling that occurs in tightly confined locations near high-latitude boundaries, and the flow along the top of our box represents the expected abyssal return flow in the oceans. Comparing the shape of the vertical density profiles in the experiments and numerical solutions to those in the oceans (figure 13*a*), we see substantial similarity, particularly in the large thermocline stratification and very small abyssal density gradients. It is not surprising that some aspects of the density structure are not identical, given that we have not allowed for the different parameter values. In particular, and with the present scaling, the abyssal density gradient in the tank is smaller than that in the

https://doi.org/10.1017/S0022112004000485 Published online by Cambridge University Press

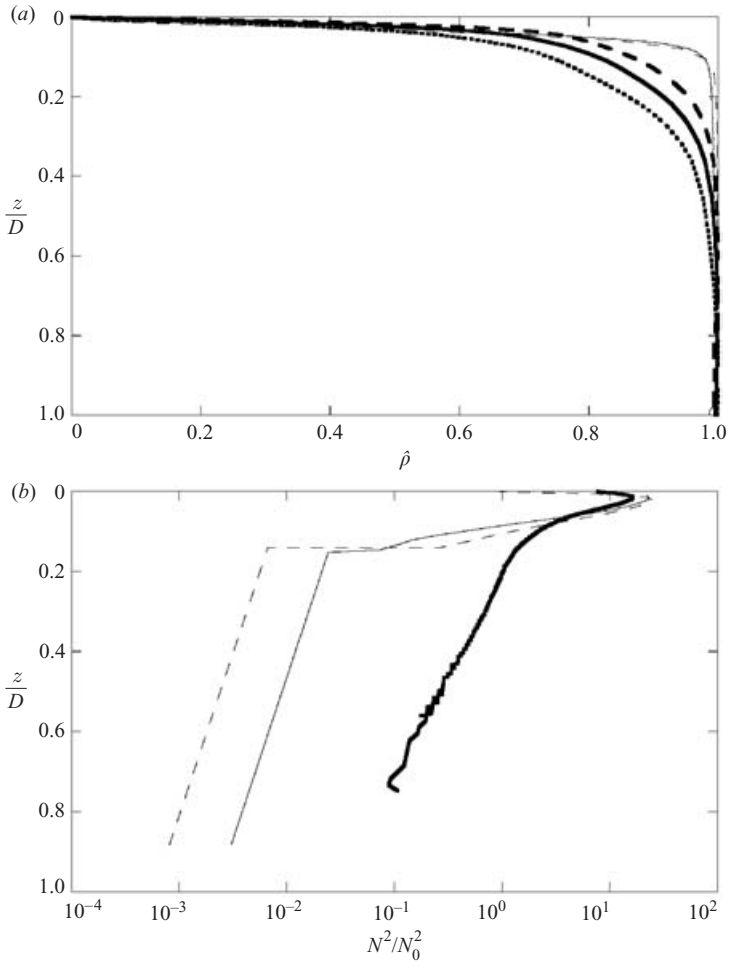


FIGURE 13. Vertical profiles of (*a*) dimensionless density, $\hat{\rho}$, and (*b*) the square of normalized buoyancy frequency, N^2/N_0^2, from an experiment (fine solid line), the corresponding numerical solution (fine dashed line), and the oceans (bold lines). For easy comparison of shape, depth has been normalized by the total depth D ($z=0$ being the forcing boundary in each case). The dimensionless density has been set to $\hat{\rho}=0$ at the forcing boundary and $\hat{\rho}=1$ at the opposite horizontal boundary and $N_0^2=g\Delta\rho/\rho D$, where $\Delta\rho$ is the top-to-bottom density difference. The ocean depth is taken to be 4000 m, giving $N_0^2=7.41\times10^{-6}\,\mathrm{rad^2\,s^{-2}}$. In (*a*), the laboratory curve is a horizontal average of vertical profiles taken at five locations along the box, the numerical solution is a horizontal average over the box (run 3 in table 1), and the ocean profiles are potential density averages over the northern hemisphere (bold dashed line), southern hemisphere (bold dotted line) and global ocean (bold solid line). Ocean data comes from the Levitus 1994 data set (http://iridl.ldeo.columbia.edu/SOURCES/.LEVITUS94/). In (*b*), the laboratory and numerical profiles are taken at the centre of the box ($x=0.625$ m). The temperature gradient outside the boundary layer was calculated by differentiating an exponential fit to the data, while the gradient in the boundary layer was found by differencing the data. This approach provides a reliable description of the data except at the edge of the boundary layer where there is an artificial discontinuity in gradient. The ocean data is a global mean and is taken from Peixoto & Oort (1992, p. 197).

oceans. The two-dimensional numerical solution gives a still smaller density gradient. The abyssal gradient (figure 13*b*), though small compared to that in the boundary layer, is dynamically important since it is required for the plume to penetrate through

https://doi.org/10.1017/S0022112004000485 Published online by Cambridge University Press

the full depth of the basin. This gradient also supports internal waves and influences turbulence.

Application of the convective scaling of § 2 to the ocean predicts a thermocline thickness ($h \sim 60\,\mathrm{m}$) that is much smaller than the measured depth ($\sim 1000\,\mathrm{m}$), a temperature difference ($\delta T \sim 13\,^{\circ}\mathrm{C}$) about half the observed value and a volume flux ($V \sim 4 \times 10^{7}\,\mathrm{m^3\,s^{-1}}$) that is somewhat larger than the estimated net poleward flux of surface waters (of order $1 \times 10^{7}\,\mathrm{m^3\,s^{-1}}$ in each hemisphere, Houghton *et al.* 1996, p. 212). Here, we have taken $L = 10^{7}\,\mathrm{m}$, $\alpha = 2 \times 10^{-5}\,\mathrm{K^{-1}}$ in the deep cold interior, a total heat flux of $2 \times 10^{15}\,\mathrm{W}$ in each hemisphere, giving an average surface flux $F_{_T} = 20\,\mathrm{W\,m^{-2}}$ at low latitudes, and the measured turbulent mixing coefficient $\kappa_{_T} = \nu = 10^{-5}\,\mathrm{m^2\,s^{-1}}$. Hence, the boundary-layer scaling of horizontal convection apparently fails to describe the ocean thermocline. We note that the geostrophic scaling leads to the dependence $V \sim \kappa_{_T}^{2/3}$ and $V \sim \delta T^{1/3}$, and a thermocline thickness of order 100 m. This scaling is found to be consistent with the predictions of a class of three-dimensional general circulation models (Park & Bryan 2000) (although another GCM in which the thermocline thickness is allowed to vary with latitude yields the diffusivity dependence $V \sim \kappa_{_T}^{1/3}$, Bryan 1987). On the other hand, we observe that the boundary-layer thickness in figure 13 appears to scale with the total water depth.

The laboratory model is of most relevance to the dynamics of the deep circulation, where buoyancy forces may drive sinking and dominate the equatorward abyssal flow. The laboratory model demonstrates how the mass flux generated in the boundary layer must be accommodated both in the sinking plume and in the interior. In the latter, a Munk-like (1966) balance between vertical advection and diffusion is required with interior diffusivity much greater than the molecular diffusivity. The uptake of buoyancy is, however, governed by the molecular diffusivity because the boundary-layer flow is characterized by low Reynolds number and bounded by a no-slip surface. Were the molecular diffusivity ($\kappa = \kappa_{_T} = 1.4 \times 10^{-7}\,\mathrm{m^2\,s^{-1}}$) also relevant to uptake of buoyancy at the ocean surface, the dissipation prediction (1.1) implies $\overline{\epsilon} = 1 \times 10^{-12}\,\mathrm{m^2\,s^{-3}}$, using the measured difference of $3.1\,\mathrm{kg\,m^{-3}}$ between the average bottom density and the average surface density, and an ocean depth of $D = 4000\,\mathrm{m}$. This value of $\overline{\epsilon}$ is approximately 100–1000 times smaller than values observed in the ocean interior. If the energy in the interior is to be supplied by buoyancy forcing alone, this suggests that the diffusivity characterizing the uptake of buoyancy at the ocean surface is 100–1000 times greater than the molecular value. This view is qualitatively consistent with the presence of a turbulent surface layer in the oceans (energized primarily by winds) and measured upper-ocean vertical diffusivities of order 10^{-5}–$10^{-4}\,\mathrm{m^2\,s^{-1}}$. However, when the uptake is by molecular diffusion, we still predict levels of abyssal turbulence comparable to that in the laboratory. Below a depth of 2000 m, the buoyancy frequency $N_i < 10^{-3}\,\mathrm{s^{-1}}$, $\nu = 10^{-6}\,\mathrm{m^2\,s^{-1}}$ and the ratio $\overline{\epsilon}/\nu N_i^2 > 1$. This value becomes larger if we use the smaller local values of N_i at greater depths, and is similar to the laboratory value. A spatial variability of dissipation rates might again locate most of the oceanic dissipation in the sinking plumes rather than in the interior. However, both the similarity of the dimensionless volume-averaged dissipation rate to that in the experiments and the coupling of $\overline{\epsilon}$ with the rate of buoyancy uptake (whether by molecular or turbulent processes) at the surface, suggest the possibility of a steady-state ocean that can adjust the rate of buoyancy-driven abyssal mixing such that the downward diffusive heat flux matches the cooling flux to the deep ocean in the plume. This intriguing aspect of the flow will be expanded on in another article.

The observed sensitivity to initial conditions of the adjustment toward the final equilibrium state reflects the fine balance required for the vertical plume to penetrate

https://doi.org/10.1017/S0022112004000485 Published online by Cambridge University Press

the full depth of the box. Thus, we speculate, as many other authors have done, that changes in the ocean MOC resulting from changes in surface forcing might cause a reduction in the penetration depth of the high-latitude sinking if the net surface heat (or water) flux is such as to decrease the ocean surface density with time (e.g. by adding fresh water). Barring further changes in boundary conditions there will be an eventual return to full depth convection when the ocean has adjusted to make the net heat and water fluxes vanish. However, the transient flow pattern can persist for very long times, of the order of the diffusion time through a significant fraction of the ocean depth. There is potential for further examination of transient adjustment and cases with unsteady forcing.

Our experiments indicate that vertical convective mixing (which carries no net vertical mass flux) in the boundary layer can deepen with distance toward the destabilized end of the basin (increasing latitude in the oceans) until all of the (poleward) mass flux in the boundary layer is involved. The inclusion of the full mass flux in the mixed layer is a consequence of the vigour of the high-Rayleigh-number circulation, in which heat transfer from the destabilizing boundary is dominated by convection rather than conduction (with diffusion remaining dominant in the stably stratified region of the boundary layer). In a steady mean thermal state, all of the cooled boundary layer must be reheated by the time it reaches the plume. At the high-latitude end of the box, the convection deepens very rapidly because it penetrates through the full depth of the thermocline and into the much smaller interior gradient. At this location, the horizontal flow also feeds into a bulk downwelling and, in the two-dimensional non-rotating case, the 'deep convection' and downwelling are coincident. Further experimental work will add Coriolis effects and examine the possibility of separate sites for deep convection and downwelling in three-dimensional geostrophic circulation.

We thank Tony Beasley and Chris Morgan for construction of equipment and laboratory assistance, and Brad Ferguson for help with photography. The Australian Partnership for Advanced Computing National Facility provided CPU time and we thank Stuart Midgley for technical assistance with using the supercomputer.

REFERENCES

Barry, M. E., Ivey, G. N., Winters, K. B. & Imberger, J. 2001 Measurements of diapycnal diffusivities in stratified fluids. *J. Fluid Mech.* **442**, 267–291.

Batchelor, G. K. 1967 *An Introduction to Fluid Dynamics*. Cambridge University Press.

Bryan, F. 1987 Parameter sensitivity of primitive equation ocean general-circulation models. *J. Phys. Oceanogr.* **17**, 970–985.

Bryan, K. & Cox, M. 1967 A numerical investigation of oceanic general circulation. *Tellus* **19**, 54–80.

Carslaw, H. S. & Jaeger, J. C. 1959 *Conduction of Heat in Solids*, 2nd edn. Oxford University Press.

Colin de Verdiere, A. 1988 Buoyancy driven planetary flows. *J. Mar. Res.* **46**, 215–261.

Condie, S. A. & Griffiths, R. W. 1989 Convection in a rotating cavity: modelling ocean circulation. *J. Fluid Mech.* **207**, 453–474.

Condie, S. A. & Ivey, G. N. 1988 Convectively driven coastal currents in a rotating basin. *J. Mar. Res.* **46**, 473–494.

Dalziel, S. B., Hughes, G. O. & Sutherland, B. R. 2000 Whole-field density measurements by 'synthetic schlieren'. *Exps. Fluids* **28**, 322–335.

Hart, J. E. 1971 Stability of the flow in a differentially heated inclined box. *J. Fluid Mech.* **47**, 547–576.

https://doi.org/10.1017/S0022112004000485 Published online by Cambridge University Press

Honji, H., Taneda, S. & Tatsuno, M. 1980 Some practical details of the electrolytic precipitation method of flow visualisation. *Rep. Res. Inst. Appl. Mech. (Japan)* **28**, 83–89.

Houghton, J. T., Meira Filho, L. G., Callander, B. A., Harris, N., Kattenberg, A. & Maskell, K. 1996 *Climate Change 1995: The Science of Climate Change*. Cambridge University Press.

Huang, R. X. 1999 Mixing and energetics of the oceanic thermohaline circulation. *J. Phys. Oceanogr.* **29**, 727–746.

Jeffreys, H. 1925 On fluid motions produced by differences of temperature and humidity. *Q. J. R. Met. Soc.* **51**, 347–356.

Leonard, B. 1984 Third-order upwinding as a rational basis for computational fluid dynamics. In *Computational Techniques and Applications: CTAC-83* (ed. J. Noye & C. Fletcher), pp. 106–120. Elsevier.

Manins, P. C. & Turner, J. S. 1978 The relations between the flux ratio and energy ratio in convectively mixed layers. *Q. J. R. Met. Soc.* **104**, 39–44.

Marotzke, J. 1997 Boundary mixing and the dynamics of three-dimensional thermohaline circulations. *J. Phys. Oceanogr.* **27**, 1713–1728.

Marotzke, J. & Scott, J. R. 1999 Convective mixing and the thermohaline circulation. *J. Phys. Oceanogr.* **29**, 2962–2970.

Munk, W. 1966 Abyssal recipes. *Deep-Sea Res.* **13**, 707–730.

Munk, W. & Wunsch, C. 1998 Abyssal recipes II: energetics of tidal and wind mixing. *Deep-Sea Res.* **45**, 1977–2010.

Paparella, F. & Young, W. R. 2002 Horizontal convection is non-turbulent. *J. Fluid Mech.* **466**, 205–214.

Park, Y. & Bryan, K. 2000 Comparison of a thermally driven circulation from a depth-coordinate model and an isopycnal model. Part I: scaling law sensitivity to vertical diffusivity. *J. Phys. Oceanogr.* **30**, 590–605.

Park, Y. & Bryan, K. 2001 Comparison of a thermally driven circulation from a depth-coordinate model and an isopycnal model. Part II: The difference and structure of the circulations. *J. Phys. Oceanogr.* **31**, 2612–2624.

Park, Y. G. & Whitehead, J. A. 1999 Rotating convection driven by differential bottom heating. *J. Phys. Oceanogr.* **29**, 1208–1220.

Pedlosky, J. 1979 *Geophysical Fluid Dynamics*. Springer.

Peixoto, J. P. & Oort, A. H. 1992 *Physics of Climate*. American Institute of Physics.

Pierce, D. W. & Rhines, P. B. 1996 Convective building of a pycnocline: laboratory experiments. *J. Phys. Oceanogr.* **26**, 176–190.

Pierce, D. W. & Rhines, P. B. 1997 Convective building of a pycnocline: a two-dimensional nonhydrostatic numerical model. *J. Phys. Oceanogr.* **27**, 909–925.

Rossby, H. T. 1965 On thermal convection driven by non-uniform heating from below: an experimental study. *Deep-Sea Res.* **12**, 9–16.

Rossby, T. 1998 Numerical experiments with a fluid heated non-uniformly from below. *Tellus* **50**, 242–257.

Ruddick, B. R. & Shirtcliffe, T. G. L. 1979 Data for double diffusers: physical properties of aqueous salt-sugar solutions. *Deep-Sea Res.* **26A**, 775–787.

Stommel, H. 1962 On the smallness of sinking regions in the ocean. *Proc. Natl Acad. Sci.* **48**, 766–772.

Sutherland, B. R., Dalziel, S. B., Hughes, G. O. & Linden, P. F. 1999 Visualization and measurement of internal waves by 'synthetic schlieren'. Part 1. Vertically oscillating cylinder. *J. Fluid Mech.* **390**, 93–126.

Warren, B. A. 1981 Deep circulation of the world ocean. In *Evolution of Physical Oceanography* (ed. B. A. Warren & C. Wunsch), pp. 6–41. MIT Press, Cambridge, MA.

Winton, M. 1995 Why is the deep sinking narrow? *J. Phys. Oceanogr.* **25**, 997–1005.

Wright, D. G. & Stocker, T. F. 1991 A zonally averaged ocean model for the thermohaline circulation 1: Model development and flow dynamics. *J. Phys. Oceanogr.* **21**, 1713–1724.

Wunsch, C. & Ferrari, R. 2004 Vertical mixing, energy and the general circulation of the oceans. *Annu. Rev. Fluid Mech.* **36**, 281–314.

https://doi.org/10.1017/S0022112004000485 Published online by Cambridge University Press